Archive of Applied Mechanics (2025) 95:101
https://doi.org/10.1007/s00419-025-02803-w

ORIGINAL

Tom Schneider · Jens Gibmeier · Markus Kästner

Experimental and numerical investigation of the evolution of residual stresses under cyclic mechanical loading

Received: 21 June 2024 / Accepted: 18 March 2025

Abstract Forming-induced residual stresses highly influence the performance of metallic engineering components. They offer great potential particularly for increasing fatigue life by targeted introduction of compressive residual stresses in failure-critical areas. However, this only holds true if one can understand and predict the change of residual stresses under cyclic mechanical loading and thus ensure their stability. In the present paper, we introduce a combined experimental and numerical approach for the investigation of residual stress evolution under cyclic mechanical loading. Therefore, a suitable experiment is conceptualized and realized using a 4-point bending setup. The initial plastic deformation of each specimen is followed by a certain number of load cycles and experimental residual stress analyses. From this, a course of residual stresses over the fatigue life is constructed. In order to simulate the determined change in residual stresses, a cyclic plasticity model is proposed that takes into account the nonlinear kinematics due to the large deflection of the beam. A parametrization algorithm is presented, which employs a global optimization strategy using uniaxial stress–strain data from various parametrization experiments. The final comparison of experimental and numerical results shows a qualitative agreement. Their stabilization level after a few thousand load cycles can be predicted.

Keywords Residual stress · Cyclic mechanical loading · Cyclic plasticity · Fatigue loading

1 Introduction

The fatigue life is of outstanding importance for the design and the dimensioning of technical components. Understanding and especially improving the structural durability of such parts enable the construction of cost-efficient and lightweight structures. Recently, for improving the properties and in particular the fatigue life of metallic components manufactured by forming processes, the targeted use of residual stresses was subject of extensive research [1–3]. Forming-induced residual stresses are equilibrium stress states that may originate from the elastic–plastic forming history during the manufacturing process and remain in the material even

T. Schneider · M. Kästner
Chair of Computational and Experimental Solid Mechanics, TUD Dresden University of Technology, Dresden, Germany

J. Gibmeier
Institute of Applied Materials - Materials Science and Engineering, Karlsruhe Institute of Technology, Karlsruhe, Germany

M. Kästner
Dresden Center for Computational Materials Science (DCMS), Dresden, Germany

M. Kästner (✉)
Dresden Center for Fatigue and Reliability (DCFR), Dresden, Germany
E-mail: markus.kaestner@tu-dresden.de

Published online: 17 April 2025

after unloading the structure. This macroscopic definition of residual stresses used in the present contribution, namely that residual stress is approximately homogeneous across several grains, corresponds to the type I residual stresses definition [4,5]. Additionally, type II and type III residual stresses exist, which are assumed to be homogeneous over smaller material length scales, i.e., a (partial) grain and atomic lattice spacing, respectively [6,7]. A variety of factors, including crystallographic orientation, grain size, phase transformations, and dislocation dynamics, critically influence the development of these stresses. In technical terms, the resulting residual stress emerges from a complex superposition of all types of residual stresses at the different length scales. However, given that our study is focused on the type I residual stress perspective in engineering applications, a detailed analysis and modeling of type II and III residual stresses is beyond the scope of the present work. For further details, the reader is referred to the literature, for example, [3,7,8].

Historically, industrial applications have predominantly used components in which the residual stresses were largely reduced to a minimum, employing conventional practices like post-forming heat treatments for residual stress reduction [2]. This stems from the widely accepted understanding that residual stresses, particularly tensile residual stresses, adversely affect performance, leading to issues such as component distortion or decreased fatigue life, e.g., in welded joints. However, residual stresses do not always necessarily have negative effects on part performance [8,9]. That especially the fatigue life can be increased by compressive residual stresses is widely known [10,11]. This is due to the fact that compressive residual stresses in failure-critical areas superimpose load-induced tensile stresses, resulting in a lower effective stresses, counteracting the initiation and development of fatigue cracks. Exemplary, Kühne et al. [12] and Guilleaume et al. [13] showed that the fatigue life of parts manufactured by cross-rolling can be improved by an adjusted rolling path during the manufacturing process, which leads to compressive residual stresses in the process induced, failure-critical notch. Seiler et al. [14] outlined the retarding effect of compressive residual stresses on fatigue crack growth and a suitable modeling strategy using a phase-field model for fatigue fracture. More examples for the beneficial use of residual stresses can be found in the literature, e.g., [3,8]. However, the positive effect of forming-induced residual stresses requires that they are retained in the component during its service life. Especially homogeneous plastic deformation after the forming process may result in the reduction of residual stress due to stress redistribution and the resulting homogeneous stress and strain state [3]. Cyclic loading beyond the yield strength of the material can therefore affect the residual stress state, so it is crucial to understand the mechanisms and extent to which residual stresses change in situations involving plastic deformation. In the context of fatigue, this understanding is decisive in order to assess whether the component can still withstand the loads for which the induced residual stresses were originally designed. Consequently, there is great practical importance to consider and investigate the combined formation of residual stresses during the process and the subsequent change under cyclic mechanical loading, which is referred to below as *residual stress evolution*.[1]

The investigation of formation and evolution of residual stresses can be carried out experimentally or numerically, whereby the combined approach of numerical modeling with the finite element (FE) method and experimental model validation in particular promises a valuable contribution with regard to the transferability of the findings. For modeling, one has to consider that macroscopic formation of residual stresses directly results from the quasi-static elastic–plastic loading, and that the evolution of residual stress is affected by the material's transient behavior, encompassing cyclic hardening or softening, and, more broadly, its cyclic plasticity, incorporating phenomena such as ratcheting or mean stress relaxation. Hence, modeling the combined formation and evolution of residual stresses requires a material model accounting for cyclic plasticity. Numerous material models for cyclic plasticity exist. In particular, models employing nonlinear kinematic hardening rules have demonstrated effectiveness in accurately predicting complex load scenarios, especially under asymmetrical loading conditions, e.g., ratcheting or mean stress relaxation [16]. Beginning with the classical model proposed by Chaboche [17,18], which is rooted in the concepts introduced by Armstrong and Frederick [19], extensions have been developed by Ohno and Wang, encompassing their Model I and II [20,21]. Additionally, contributions from Jiang and Sehitoglu [22,23], Abdel-Karim and Ohno [24], and Döring et al. [25,26] have further enriched the understanding and modeling of the transient behavior of metals. This outline is by no means complete, as numerous models exist and new ones are constantly being added. A thorough review on the topic can be found in [26–28]. However, despite the vast array of different models, they all share the aim of accurately reproducing material behavior under complex loading situations and many

[1] Note that a specific method for mitigating residual stress involves the use of vibrations, commonly referred to as vibrational stress relief (VSR) [15]. In the broadest sense, this approach can be viewed as inducing changes in residual stress through cyclic loading. However, this high-cycle, low-load technique, whose mechanisms and effects are controversially discussed in the literature, is beyond the scope of this study, which focuses on macroscopic plastic loading.

thousands of load cycles to provide predictions for stresses and strains, e.g., for a fatigue life analysis using the local strain approach [25]. It therefore seems reasonable that these models should also be able to predict the development of residual stresses under cyclic loading.

The application of plasticity models for the prediction of forming induced macroscopic residual stress is state of the art. With a properly parameterized process simulation and adequate material modeling researchers have shown that the prediction of residual stresses is possible, e.g., for bulk forming [29,30] or sheet forming [31, 32]. Furthermore, several studies have predicted residual stresses at lower material scales, specifically type II and type III residual stresses, e.g., Simon et al. [33], Behrens et al. [34], Uebing et al. [35], and Salvati and Korsunsky [36]. However, loading situations that go beyond the initial phase of residual stress formation have not yet been the subject of extensive research. The interaction of cyclic loading after the forming process with the residual stresses is usually not taken into account. Exemplary, Dureau et al. [37] investigated residual stresses induced by laser shock peening during a few load cycles in uniaxially loaded specimens. They used a layer-wise calibrated Chaboche model to capture the depth-dependent change of the residual stress profile in layers close to the surface. Franceschi et al. [38] investigated forming-induced residual stresses at high loads for low numbers of cycles using two separate material models for the formation and evolution of residual stresses. McClung [39] presented a comprehensive literature review on the stability and evolution of residual stresses under fatigue loading, which is mainly based on experimental data. In this context, different materials are examined, with particular attention given to near-surface residual stress fields resulting from processes such as surface treatments, welding, or machining. Xie et al. [40] and Wang and Qian [41] analyzed the residual stress evolution in welded joints using experimental and numerical methods. The analysis of residual stresses in mooring chains has been conducted in Zarandi and Skallerud [42]. Therein, the simulation of the residual stress in the vicinity of a corrosion pit using a Chaboche-type cyclic plasticity model revealed that cyclic plasticity may lead to residual stress change especially in the early stages of cyclic loading. Further investigations on incremental sheet forming processes, representing cyclic loading situations in the broadest sense, have been conducted, e.g., in studies such as [31,32].

It seems that the formation and evolution of residual stresses have so far mainly been described by two separate models, cf. [37,38,40,41]. This leads to the disadvantage that a transfer of the forming simulation results to the cyclic simulation is needed, which may be associated with a certain error, e.g., regarding the used FE mesh or the initial conditions for internal variables. There are also studies, e.g. [42], in which a single model is used. However, in [42] a rather complex stress–strain state is analyzed, which limits the transferability of the studies to a certain extent. Hence, the simulation part of this paper attempts to capture both phenomena of residual stress generation and evolution under cyclic loading in a single model for a reference stress–strain state, which is easy to analyze experimentally and numerically.

In the following, we present an approach to investigate the combined buildup of forming-induced residual stresses and their evolution under cyclic mechanical loading experimentally and numerically in a simple test setup. We focus on a 4-point bending test, since a pure bending state is the easiest way to induce residual stresses by forming. The residual stresses are determined experimentally using the incremental hole drilling method and their development over fatigue life is investigated. For simulation, a cyclic plasticity model is employed, which closely follows the work of Jiang and Sehitoglu [22,23] and Döring et al. [25,26]. Due to the high deflection of the specimens observed during experiments, we have extended this material model to take into account the resulting nonlinear kinematics. The subsequent parametrization of the material model is carried out using an optimization scheme for uniaxial loading. The parametrized model's performance in comparison with the experiment is evaluated, and arising challenges are discussed. In order to follow the idea of a benchmark experiment, all experimental data generated in the following is published as open access repository in Schneider at al. [43] to allow the community to compare their own models for residual stress prediction.

The present paper is structured as follows: In Sect. 2, the designed experiment is presented, and the test setup is described. Also, gained results of the experimental residual stress analysis are discussed. In Sect. 3 the material model, which is used afterward for the numerical simulation, is outlined. Additionally, the parametrization of the model is presented. With this model, numerically gained results are revealed and compared to the experiments in Sect. 4. Lastly, the overall procedure and findings are summarized in Sect. 5.

2 Experimental investigation

The subsequent sections provide a detailed account of the experimental investigation. Section 2.1 describes the experimental setup, while Sect. 2.2 outlines the adopted loading procedure. The effects of both initial

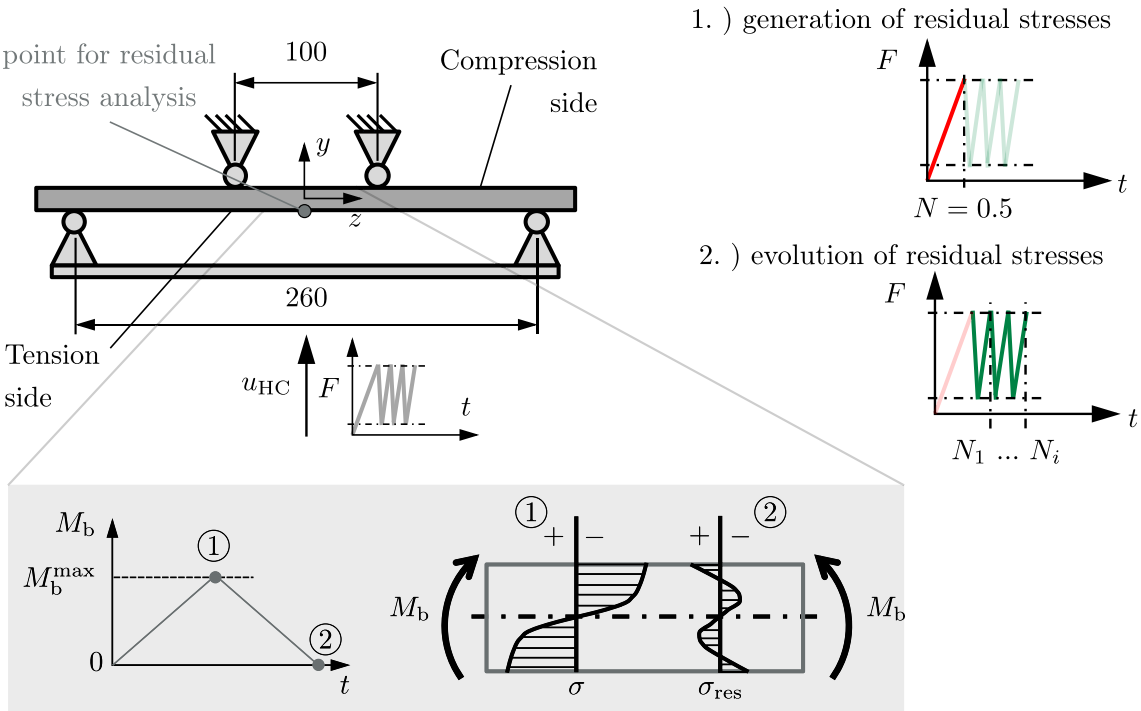

Fig. 1 Schematic setup of the setup (left) and the employed two-stage loading procedure (right) for generation and evolution of residual stresses. Dimensions in mm. The gray box shows the qualitative stress curve resulting from the constant bending moment M_b between the inner supports after a loading ① and unloading process ②. The used support structures are steel cylinders with ø20mm. The specimen is loaded by an initial load (——), which is followed by cyclic loading (——) of the structure using a load ratio of $R_\sigma = 0.1$. After residual stress generation during the first load cycle $N = 0.5$, the tests are stopped at various load cycle numbers N_i for experimental residual stress analysis

and cyclic loading on the development and evolution of residual stresses are presented in Sects. 2.3 and 2.4, respectively. Finally, Sect. 2.5 discusses the outcomes of the experimental residual stress analysis.

2.1 Experimental setup

The design and construction of an experimental setup for the investigation of residual stress generation and evolution under cyclic mechanical loading was a major task of the present contribution, since forming-induced residual stresses can occur in various spatial distributions and result from arbitrarily complex loading situations. In order to facilitate the evaluation for the present investigation, a generalized test setup needed to be designed. This setup was developed such that it fulfills the following requirements:

- A general two-stage procedure: First, the residual stresses need to be induced by forming in a suitable way. Second, the specimen should be loaded cyclically in order to investigate the changes of the initial residual stresses.
- An approach which is as simple as possible for the general setup, the experimental residual stress analysis, the specimen geometry, the loading situation and also the resulting stress–strain field.
- A load level that leads to macroscopic plastic deformation in order to evaluate the effect of cyclic plasticity on residual stresses.

These specifications for the setup development aim to streamline the evaluation of subsequent experimental results and to establish a foundation for potential comparisons among various numerical modeling strategies that may be utilized by the mechanics community. The initially induced residual stresses as well as their evolution under the subsequent cyclic mechanical loading can be determined experimentally and may be used to evaluate the prediction quality of macroscopic numerical models for residual stresses under cyclic loading.

Applying the requirements, we constructed a 4-point bending setup with the geometric specifications depicted in Fig. 1. Similar setups are presented in the literature [38,41,44]. The 4-point bending test is par-

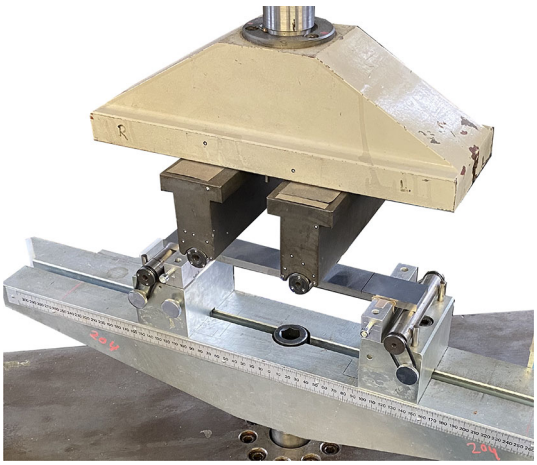

Fig. 2 Photograph of the realization with the hydraulic cylinder located below the experimental setup

ticularly suitable for the investigations since it results in a large domain of the beam with constant bending moment. Additionally, due to the flat specimen surface, the experimental residual stress analysis is simplified. The constant bending moment leads to a linearly distributed strain profile across the thickness of the beam. Due to plastic deformation in layers close to the surface, the typical nonlinear stress profile emerges, see ① in Fig. 1. After unloading, see ② in Fig. 1, the typical double s-shaped residual stress profile can be observed. Tensile residual stresses result on the compression side of the beam, while compressive residual stresses prevail on the tension side of the beam. Following the conduction of pre-tests, simple cuboid specimen with dimensions $8 \times 35 \times 270\,\mathrm{mm}^3$ was determined for further testing. A high-strength steel 42CrMo4+QT (1.7225 or SAE4140) in quenched and tempered condition is used. The specimens are machined out of 8 mm flat steel whereby the surface was fine ground and edges were polished by hand in order to avoid surface effects on the fatigue life. The support structures are ø20mm steel cylinders on both sides of the beam. Aligners that are coated on the inside with Teflon strips prevent the beam from accidentally slipping off the supports. An uniaxial servo hydraulic cylinder is used to load the bending specimen. During the tests, the test rig operates in force control and has a force sensor with a load capacity of 40 kN. By default, the force signal and the position signal of the cylinder are recorded during the tests.

2.2 Loading procedure

In the setup, forming-induced residual stresses are generated by initial bending of the specimens with $F_{\max} = 15\,\mathrm{kN}$. Following ideas of Kühne et al. [12], this first bending is termed as *first load cycle*. Directly after the initial loading, the cyclic loading begins, see $F(t)$ plot in Fig. 1. The cyclic loading situation was chosen to be a constant amplitude loading with a load ratio of $R_\sigma = 0.1$, loading frequency of 1 Hz and a maximum force of $F_{\max} = 15\,\mathrm{kN}$. The imposed mean load prevents relative motion between the beam and its supports, which might otherwise occur under the influence of alternating loads. For the investigation of the residual stresses and their evolution under cyclic loading, the cyclic tests need to be stopped after various defined numbers of load cycles before fatigue failure. After the test stopped for a specimen, it undergoes experimental residual stress analysis using the common hole drilling method, see later Sect. 2.5. This approach has the advantage that for comparison of experimentally determined residual stresses and simulated results not only data point from the very surface are considered, but a residual stress depth distribution with a rather large depths range up to about a millimeter. By this mean, the comparison between experiment and simulation is statistically much better supported. Combining results from all specimens, a $\sigma_{\mathrm{res}} - N$ plot can be created which shows the evolution of the residual stresses under cyclic loading. Since hole drilling is a destructive analysis method, each load cycle number at which the test is stopped requires a separate specimen. It is assumed that the results obtained for different samples are comparable since they were made from the same sheet metal. To simplify the interaction with the provided experimental data, specimen numbers are introduced in the format: #... . They correspond to the data set published as open access repository in [43] and are assigned a load cycle number in later Table 1 (Fig. 3).

Fig. 3 Screenshot of the ARAMIS definition for the bending test of the first load cycle. The area of evaluation was chosen such that it is located within the inner supports. Also visible are the supports used and the aligners, which are coated with Teflon on the inside

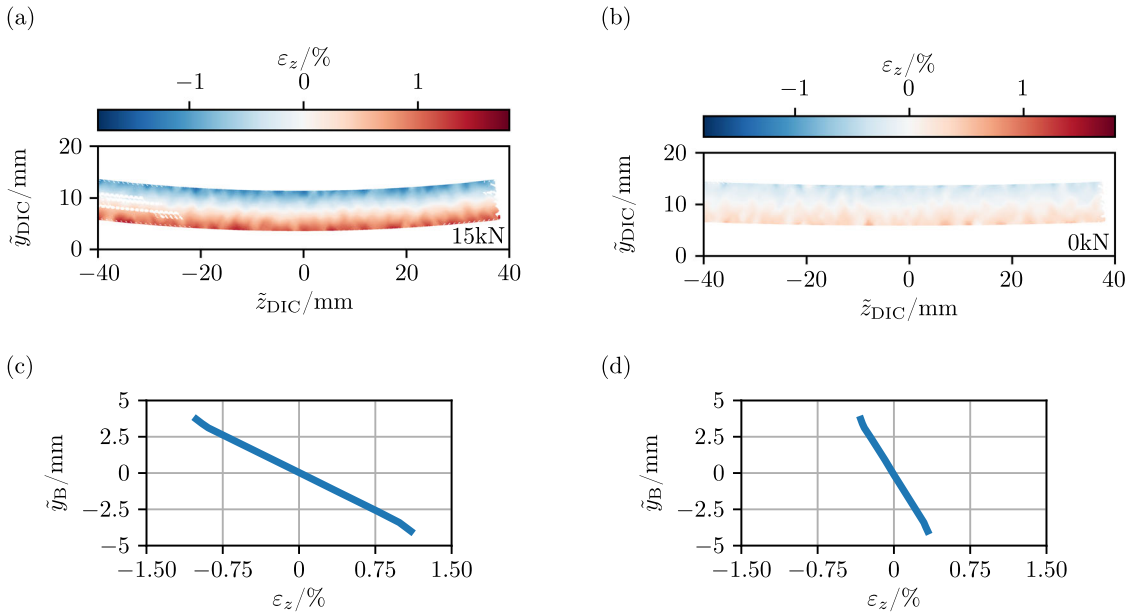

Fig. 4 Experimental results from the DIC measurement of the first load cycle for specimen #0007. Depicted is the spatial logarithmic strain ε_z. **a** strain state at $F_{\max}$ and **b** strain state after unloading following the initial load cycle. The absolute position of the coordinate system $\tilde{y}_{\mathrm{DIC}} - \tilde{z}_{\mathrm{DIC}}$ was chosen automatically by the DIC system. In **c** and **d** the strain profile averaged over the beam length of constant M_{b} is plotted over the beam height $\tilde{y}_{\mathrm{B}}$ in (c) fully loaded and (d) unloaded state, respectively

2.3 Initial bending–experimental results

Following the above discussed procedure, see Fig. 1, the experimental results after the first load cycle, are discussed. The results of cyclic bending can be found in the later Sect. 2.4. For analyzing the initial loading, not only the default sensors of force and position are used. For two specimens, the initial deformation of the first load cycle was analyzed with 3D digital image correlation (DIC) using a GOM® ARAMIS system and the accompanying processing software. These specimens are used in Sect. 2.5 for the analysis of the residual stresses after the initial load cycle. The DIC system was positioned such that it looked sideways at the specimen, capturing the motion in the $y-z$-plane of Fig. 1. The processed results of a representative specimen are depicted in Fig. 4. The contour plots of the logarithmic strain, automatically processed from the DIC displacement data, in Fig. 4a and b clearly underline the constant M_{b} within the inner supports. Averaging the data over the beam length yields an effective strain measure over beam height $\tilde{y}_{\mathrm{B}}$ within the domain of constant M_{b}, see Fig. 4d. This results in the expected linear strain profile over the beam height. At maximum force, the beam endures a maximum strain of approx. 1.1 % at the outer surface. In the unloaded state, a residual strain of approx. 0.4 % prevails in layers close to the surface.[2]

Following the DIC analysis, the deflection of the beam during the first load cycle is evaluated using the position data. The resulting force–deflection curve is depicted in Fig. 5a. A maximum displacement of the hydraulic cylinder u_{HC} and thus of the lower supports of approx. 16 mm are reached. After unloading, the

[2] Note that the residual strain detected via DIC has nothing in common with the experimentally determined residual stresses using the incremental hole drilling method in Sect. 2.5. It is only an effective measure of the deformation, which is determined from the lateral beam surface.

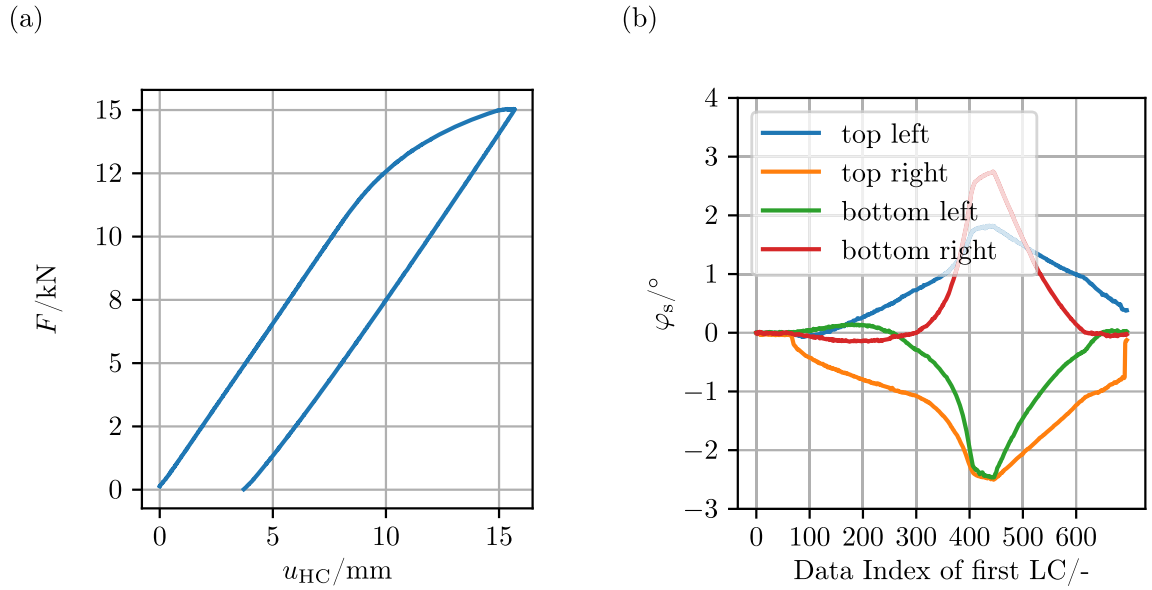

Fig. 5 Experimental deformation behavior during the initial load cycle for specimen #0007. **a** force–displacement curve from the recorded signals of the test rig. **b** the rotation of the four supports φ_s measured with the DIC system. The position of the supports is given with respect to Fig. 1

structure shows a residual displacement of approx. 4 mm. Please note that this is not the displacement in the $x - y$ symmetry plane of the beam but the displacement of the lower support structures as underlined in Fig. 1. For evaluation, one must consider that the support structures are not completely rigid. The lower steel cylinders in Fig. 2 were fixed using elastic strips. The upper supports were fixed in the top end of the test rig using elastically bedded bolts. Hence, the upper cylinders may rotate around their upper contact point with the test rig, and the lower cylinders may rotate around their axis, respectively. This was done intentionally in the design phase because otherwise constraint forces could occur that would disturb the pure bending state in the specimen, especially regarding the high deflection of the beam in maximum loading states. The rotation of the supports was additionally recorded during the first load cycle via the DIC system and is depicted in Fig. 5b. Three points on each support cylinder were used to calculate its rotation with respect to the x axis.

The data underline a rotational motion of the supports during the loading process. In maximum loading state, the absolute maximum angular deflection is lower than 3°. Converted to a horizontal displacement of the contact point between support and beam, a maximum of about 0.9 mm is obtained. As expected, the supports follow the beam's deflection toward the $x - y$ symmetry plane of Fig. 1, respectively. The influence on the comparison with numerical results especially in terms of the boundary conditions for the simulation is discussed in Sect. 4.

2.4 Cyclic loading–experimental results

The initial loading of further specimens is directly followed by cyclic loading, as described in Sect. 2.1. In a first step, the mean fatigue life of the specimens is determined experimentally in order to determine the load cycles after which further experiments are stopped for experimental residual stress analysis. For this purpose, 5 specimens are cyclically loaded in the test setup until total failure. From their test results, the mean fatigue life to crack initiation is determined. Therefore, fatigue crack initiation is assumed to take place at a relative stiffness loss of 10 % compared to the stabilized state, which is evaluated via a linear regression in logarithmic scale. The response of the specimens in terms of maximum u_{HC} during each load cycle is depicted in Fig. 6. The results show a continuous increase in the maximum deflection with accumulating number of load cycles. This is due to the load ratio chosen and is a structural ratcheting phenomenon, which has to be taken into account for the choice of material model in Sect. 3. A mean fatigue life to crack initiation of $N_f = 16.091 \times 10^3$ is found. The standard deviation of the logarithmic load cycle numbers is $s_{logN} = 0.039$ leading to a spread range of $N_{P_f=90\%}/N_{P_f=10\%} = 1.26$, which is defined as the ratio of the load cycle number for 90% probability of failure to the load cycle number for 10% probability of failure. It is quite low compared to literature data [11].

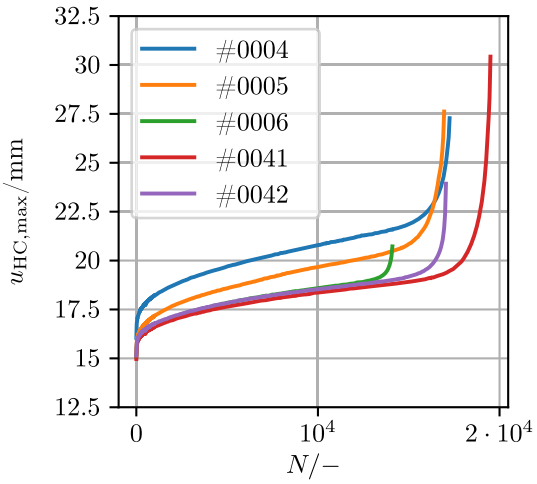

Fig. 6 Experimental result of cyclic bending test until specimen fracture. Depicted is the maximum displacement u_{HC} during each load cycle N

Table 1 Load cycles at which the tests are stopped

Load cycles N	Damage D	Specimen numbers #...
0.5	0	0007, 0008
100	0.006	0009, 0010
400	0.025	0011, 0012
800	0.05	0013, 0014
1600	0.099	0015, 0016
3200	0.199	0017, 0018
6400	0.398	0019, 0020
10000	0.621	0021
12000	0.746	0022
Tot. fracture	–	0004, 0005, 0006, 0041, 0042

The damage D_i is related to the fatigue life to crack initiation. The specimen numbers are related to the corresponding data set available in [43]

The mean experimental fatigue life to crack initiation is used to divide the fatigue life into ranges separated by discrete load cycle numbers at which the tests of further specimens are stopped for residual stress analysis. The distribution of the discrete load cycles N until unloading is depicted in Table 1. Additionally, in Table 1 the damage $D = N/N_f$ is provided. The nonlinear distribution over the fatigue life is motivated by the assumption of an initial phase with strong residual stress change followed by a stabilization phase, as observed in [38,40]. The change in displacement over the load cycles in Fig. 6 backs this suggestion.

2.5 Experimental residual stress analysis

The analysis of residual stresses after cyclic loading of the specimen was carried out using the incremental hole drilling method, initially proposed by Mathar [45]. Details on the operating principle of this method and general information on experimental residual stress analysis are comprehensively presented in the literature [7,46]. For residual stress analysis, a drilling device of type RS200, Vishay Measurements Group and for drilling a TiN-coated end mill with a nominal diameter of ø1.6mm was applied. The strain relaxations during stepwise drilling the blind hole were recorded by strain gauge rosettes of type EA-06-031RE-120 (Vishay Measurements Group), which were interconnected in a Wheatestone half bridge with temperature compensation. A carrier frequency amplifier of type PICAS 4K from Peekel Instruments was applied in this regard. Stress calculation was carried out using the differential approach and elastic constants for steel, i.e., Young's modulus $E = 210\,\mathrm{GPa}$ and Poisson's ratio $\nu = 0.28$. For smoothing of the measured strain relaxation distributions vs. drilling depth cubic spline functions were applied. By this means, it is possible to analyze the macro-residual stress distribution up to depths of about 1 mm to 1.2 mm. The experimental analyses were carried out in the symmetry plane on the

original tension side of the beam specimen. Hence, compressive residual stresses in longitudinal direction are determined. The results obtained are shown in Fig. 7.

In the following, only the residual stress in longitudinal direction σ_z is discussed. Regarding the residual stresses in transverse direction σ_x, no significant influence of the cyclic loading is observed. The state after initial loading is marked with $D = 0$ and shows the residual stress distribution with an absolute maximum of $\sigma_z \approx 260$ MPa in longitudinal direction at the surface of the beam. With accumulating number of load cycles, and hence with increasing D, one can observe an initial increase for this residual stress component. Following this initial phase, the residual stress decreases again. When approaching $D = 1$, they remain constant. Figure 8 provides a summary of the development of residual stress at the beam surface. A stabilization phase is reached quickly, which is in accordance with the findings for welded joints [40,41] and mooring chains [42] under cyclic loading. The pronounced changes in early stages of fatigue life is attributed to the material's transient behavior under cyclic loading. Here, the cyclic softening of the material in particular influences the initial change in residual stresses. For specimens close to their fatigue life of crack initiation and depending on the position of the drilled hole, a drop in residual stresses may occur due to emerging fatigue cracks, which lead to a local stress relaxation. Since only load cycle numbers clearly prior to the mean fatigue life were considered, this was not observed in the present investigation.

Cyclic loading also affects the depth profile of residual stress. For $D \leq 0.05$, one observes a higher slope in the direct vicinity of the surface compared to larger material depth, which is in line with the theoretically emerging double s-shaped profile from Fig. 1. The slope decreases with accumulating fatigue damage. After stabilization, and despite some waviness due to the evaluation method, the profile qualitatively appears to be linear. This is related to the high stresses and strains in layers close to the surface which influence the profile there through cyclic softening. Extending the widely known fact that deformation-induced residual stresses arise from inhomogeneous loading conditions, the observed results indicate that this also applies to the residual stress change under cyclic loading, which is a local phenomenon and therefore depends on the local stress–strain level and the inhomogeneity of the loading.

The scattering of the experimental results for most of the specimen is quite low. Larger differences between the two specimens used for each load cycle[3] are only visible for $D = 0$ and $D = 0.099$. It needs to be noted that in principle, the incremental hole drilling method is inherently subject to a certain degree of uncertainty, especially directly at the surface of the specimen, i.e., within the first ten micrometers [46]. In larger depth, the accuracy of the method for residual stress analysis of steel samples is in the range of 20MPa to 30MPa. Nevertheless, the in general good agreement between two specimens, each independently loaded for the same number of load cycles, indicates a qualitative level of results sufficient for the purpose intended here.

3 Modeling of residual stress evolution

Numerical analysis of the developing residual stresses and their evolution under cyclic loading can accelerate future design decisions regarding the influence of forming-induced residual stresses on engineering components. Hence, in the following a numerical modeling approach using the FE method is outlined. In Sects. 3.1 and 3.2, the overall model choice is discussed, taking into account the experimentally observed large beam deflections from Sect. 2.4. The model itself, its parameterization and gained numerical results when simulating the bending experiment are provided in Sects. 3.3, 3.4.

3.1 General aspects

Up to now, to the best of the authors knowledge, and besides the simulations discussed in Sect. 1, no straightforward investigation was carried for the simulation of combined generation of residual stresses and their evolution under cyclic mechanical loading within in one single model. In a first step, it is thus reasonable to investigate which models are able to predict the residual stresses and their change during cyclic loading in general. In the present paper, a first approach for modeling the residual stresses is discussed. Macroscopic cyclic plasticity models are considered since they allow straightforward implementation with commercial FE codes and can be used by the entire mechanics community. More complicated models incorporating damage are out of scope for the time being. They may be deployed by readers which are interested in simulating the experiment presented in Sect. 2.1. The experimental data is published in [43].

[3] For $D = 0.621$ and $D = 0.746$ only one specimen were used, respectively. Due to the stabilization effect of the cyclic loading, less influence of the specimen specific deviations was expected for higher load cycle numbers.

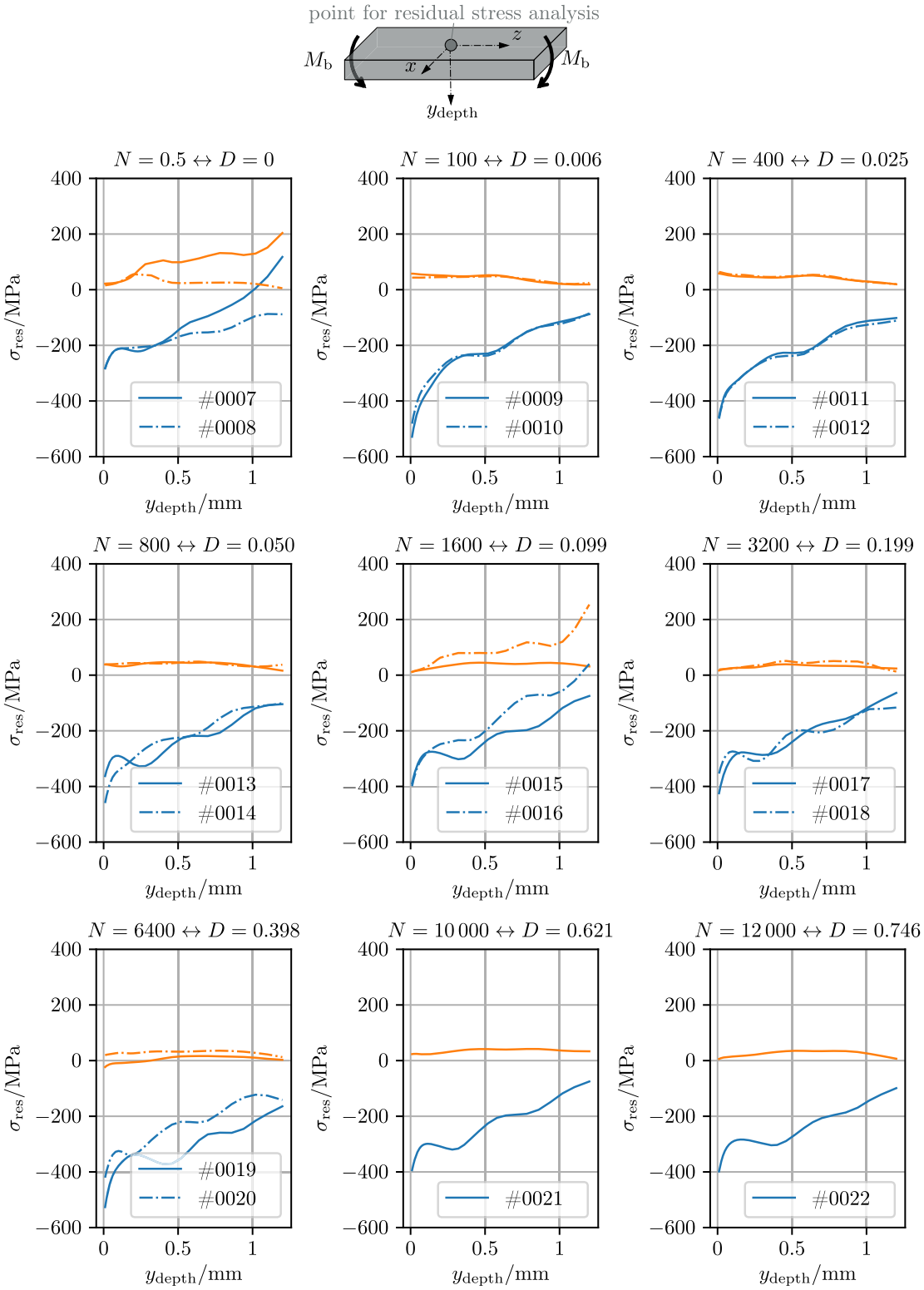

Fig. 7 Experimentally determined residual stress depth profiles after unloading the specimen at various load cycle numbers using the incremental hole drilling method. The colors represent the σ_{res} in different directions: (——) σ_z and (——) σ_x. The solid and dashed lines indicate the results of two different specimens, respectively

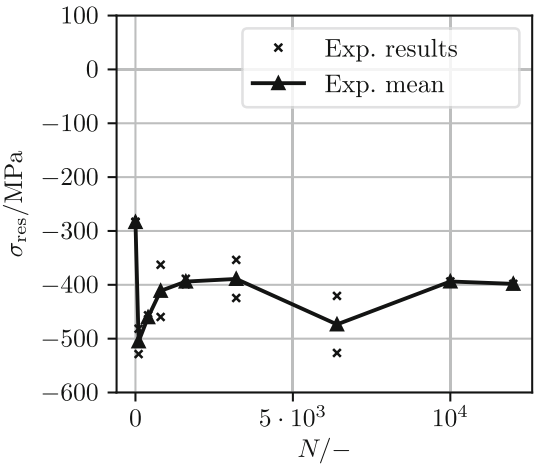

Fig. 8 Evolution of the residual stress σ_z at the surface under cyclic loading

3.2 Choice of model framework

With the aim of simulating the evolution of the residual stresses under cyclic mechanical loading using a cyclic plasticity model, the high deflection of the beam specimen, observed in the experiments from Sect. 2.4, needs to be taken into account for the analysis. Figure 6 clearly indicates a deflection of more than twice the specimen height. For this reason, approaches, which only consider small rigid body motion, typically referred to as small-strain plasticity, are ruled out. Instead, a so-called general finite strain setting is used for model development and to account for the geometric nonlinearity of the experiment, which is manly due to large local rotations. Note that the reason for choosing a general finite strain setting here is by no means that finite strains occur. They are comparably small, see Fig. 4c. This is only needed due to the existing nonlinear kinematics. Following these statements, two approaches are possible:

- plasticity models based on a hypoelastic stress relation for the elastic deformation part, which is usually based on the constitutive assumption of an additive split of the rate of deformation, whereby co-rotational modeling techniques are contained within this approach, and
- plasticity models based on a hyperelastic stress relation for the elastic deformation part, which commonly rely upon the multiplicative decomposition of the deformation gradient.

The difference between both is that for the hypoelastic approach the stress is determined from an objective stress rate, which is related to the elasticity tensor and the rate of elastic deformation, while for hyperelasticity the stress follows as partial derivative of the free energy density with respect to an appropriate elastic deformation measure. See the comprehensive paper of Brepols et al. [47] for details on implementation aspects and a practical comparison of both approaches. It is widely known that the rate-based formulation does not a priori guarantee a path-independent elastic response and thus may lead to artificial dissipation [47–49]. This is due to unphysical hysteresis in the stress–strain relationship during cyclic loading. Additionally, for shear loading with large strains, unexpected oscillating shear stress responses were observed when deploying the Jaumann objective stress rate [49]. Despite this well-known shortcomings.[4], the hypoelastic-based approach, for example in conjunction with the Jaumann or the Green-Naghdi rate, remains part of commercial FE codes, such as ABAQUS [51]. This is mainly due to their easy extensibility and the fact that they retain the structure of the small-strain formulation for plasticity assuming small elastic strains, making the implementation modular for both the case of small strains and the case of finite strains. The discussed error of the rate-based formulation is usually negligible for typical loading situations with monotonic loading, e.g., for sheet forming [47]. However, a test simulation of the present bending experiment using hypoelasticity with the Jaumann stress rate showed a significant error under cyclic loading when more than 500 load cycles were simulated. This is attributed to the known artificial dissipation of hypoelasticity-based models [48,49]. Since, according to Fig. 7, several hundreds or thousands of load cycles need to be simulated, the hypoelastic approach is ruled out for the

[4] Please note that the shortcomings were partially overcome by the introduction of the *logarithmic stress rate* It is not discussed here because, as in the case of hyperelastic-based stress relations, it would lead to a separate implementation in the FE code, making the automatically path-independent hyperelastic approaches more attractive. For more details, see, e.g., Xiao et al. [50].

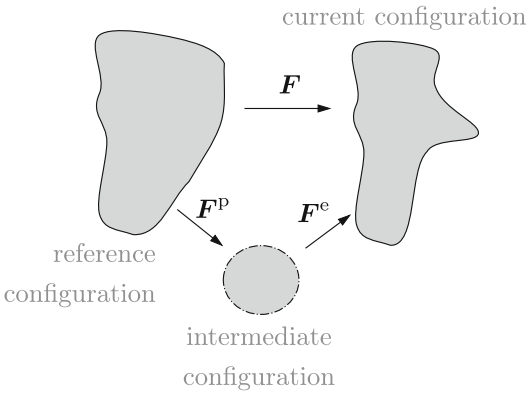

Fig. 9 Schematic representation of the configurations for nonlinear kinematics and the applied multiplicative decomposition of the deformation gradient

present investigation. Accordingly, a hyperelastic-based implementation, which leads per definition to path-independent elastic responses, is used in the following.

The choice of the actual cyclic plasticity model, operating in this framework, is motivated by the fact that various effects may influence the obtained residual stresses. Hence, a model is chosen that is theoretically capable to account for all aspects of cyclic plasticity, e.g., cyclic softening/hardening, mean stress relaxation and ratcheting. We use the small-strain model of Döring et al. [25,26], which relies on works from Jiang and Sehitoglu [22,23], as a basis. Other, even more complicated or simpler models for cyclic plasticity may be deployed by the community. Subsequently, their prediction quality can be compared to the experiments from Sect. 2.1 and to the performance of the herein chosen model.

3.3 Cyclic plasticity model for nonlinear kinematics

The cyclic plasticity model described in the subsequent section is based on the work of Döring et al. [25,26], which in turn is an extended version of Jiang and Sehitoglu's [22] model. Herein, modifications are incorporated in order to account for the geometric nonlinearities resulting from large deflections and thus large local rotations of the bending specimen from Sect. 2.1. Since no effects resulting from non-proportional loading and the sequence are expected for the present simulation, model components accounting for these influences are neglected. We apply the following mathematical notation with respect to the standard basis $\vec{e}_l$ in three-dimensional Euclidean space $\mathbb{R}^3$. Second-order tensors are denoted as bold letters, i.e., $\boldsymbol{A} = A_{ij}\,\vec{e}_i \otimes \vec{e}_j$. The inner product with single tensor contraction of two second-order tensors is denoted as $\boldsymbol{A} \cdot \boldsymbol{B} = A_{il}\,B_{lj}$, where the Einstein summation convention is applied. Double tensor contraction is written as $\boldsymbol{A} : \boldsymbol{B} = A_{ij}\,B_{ji}$. The material time derivative is abbreviated as $\dot{\boldsymbol{A}} = \frac{\mathrm{d}\boldsymbol{A}}{\mathrm{d}t}$.

The proposed model relies upon the constitutive assumption of a multiplicative decomposition of the deformation gradient [52,53]

$$\boldsymbol{F} = \boldsymbol{F}^{\mathrm{e}} \cdot \boldsymbol{F}^{\mathrm{p}} \tag{1}$$

into elastic $\boldsymbol{F}^{\mathrm{e}}$ and plastic $\boldsymbol{F}^{\mathrm{p}}$ parts, following the discussion in Sect. 3.1. Therein, $\boldsymbol{F}^{\mathrm{p}}$ can be considered as local intermediate configuration, which is mapped to the current configuration by $\boldsymbol{F}^{\mathrm{e}}$. The procedure is underlined by Fig. 9.

For $\boldsymbol{F}^{\mathrm{e}}$, the polar decomposition $\boldsymbol{F}^{\mathrm{e}} = \boldsymbol{v}^{\mathrm{e}} \cdot \boldsymbol{R}^{\mathrm{e}}$ can be applied, yielding the elastic left stretch tensor $\boldsymbol{v}^{\mathrm{e}}$ and the elastic rotation tensor $\boldsymbol{R}^{\mathrm{e}}$, respectively. The elastic logarithmic strain with respect to the current configuration is defined as

$$\boldsymbol{\varepsilon}^{\mathrm{e}} = \ln \boldsymbol{v}^{\mathrm{e}} \ . \tag{2}$$

Following Neto et al. [54], one can formulate a general hyperelastic and thus thermodynamically consistent stress relation for the Kirchhoff stress

$$\boldsymbol{\tau} = \frac{\partial \psi}{\partial \boldsymbol{\varepsilon}^{\mathrm{e}}} \ . \tag{3}$$

For the metallic material considered here, only small elastic strains arise [47,54], i.e., the free energy density ψ is defined assuming small elastic strains. Hence, the elastic part of the energy density

$$\psi^{\mathrm{e}}\left(\boldsymbol{\varepsilon}^{\mathrm{e}}\right) = \frac{\lambda}{2}\left(\operatorname{tr}\boldsymbol{\varepsilon}^{\mathrm{e}}\right)^2 + \mu\,\boldsymbol{\varepsilon}^{\mathrm{e}} : \boldsymbol{\varepsilon}^{\mathrm{e}} \tag{4}$$

with the two Lamé parameters λ, μ is deployed. This can be interpreted as the extension of linear elasticity to the finite rotations setting. The onset of yielding is modeled using a von Mises-type yield function

$$f = ||\boldsymbol{s} - \boldsymbol{X}||_{\mathrm{F}} - R\,(p) \leq 0\ . \tag{5}$$

with the deviator of Kirchhoff stress $\boldsymbol{s} = \boldsymbol{\tau} - 1/3\operatorname{tr}\boldsymbol{\tau}\,\boldsymbol{I}$ with respect to the current configuration and the second-order identity tensor $\boldsymbol{I}$. The Frobenius norm is denoted as $||\cdot||_{\mathrm{F}}$, $\boldsymbol{X}$ is the backstress tensor, describing kinematic hardening, and $R\,(p)$ is referred to as the yield stress[5] depending on the accumulated effective plastic strain p.

The plastic flow rule is defined for the plastic deformation rate $\boldsymbol{d}^{\mathrm{p}} = 1/2\left(\boldsymbol{l}^{\mathrm{p}} + \boldsymbol{l}^{\mathrm{p}\mathrm{T}}\right)$ wherein the plastic velocity gradient is defined as $\boldsymbol{l}^{\mathrm{p}} = \dot{\boldsymbol{F}}^{\mathrm{p}} \cdot \boldsymbol{F}^{\mathrm{p}-1}$. This quantity of the intermediate configuration is pushed forward to the current configuration and assigned the normality rule

$$\boldsymbol{F}^{\mathrm{e}} \cdot \boldsymbol{d}^{\mathrm{p}} \cdot \boldsymbol{F}^{\mathrm{e}-1} = \dot{p}\,\underbrace{\frac{\partial f}{\partial \boldsymbol{\tau}}}_{\boldsymbol{n}} \tag{6}$$

whereas a vanishing plastic spin, and thus isotropy [55], is assumed and the normality tensor $\boldsymbol{n}$ is introduced. One obtains the evolution equation

$$\dot{\boldsymbol{F}}^{\mathrm{p}} \cdot \boldsymbol{F}^{\mathrm{p}-1} = \dot{p}\,\boldsymbol{F}^{\mathrm{e}-1} \cdot \frac{\partial f}{\partial \boldsymbol{\tau}} \cdot \boldsymbol{F}^{\mathrm{e}}\ . \tag{7}$$

This procedure closely follows the derivation of a general hyperelastic-based plasticity model outlined in Neto et al. [54].

The evolution of the hardening variables is outlined in the following. Isotropic hardening is modeled by the phenomenologically motivated dependency

$$\dot{R}\,(p) = b\,(R_{\mathrm{T}} - R)\,\dot{p} \tag{8}$$

with the target function [25]

$$R_{\mathrm{T}} = R_0\left[1 + \frac{A_1}{(1 + b_1 p)^2}\right] \tag{9}$$

and A_1 and b_1 being material parameters [25]. Compared to [25] where three transient terms are used Eq. 9, only one is considered here in order to reduce model complexity. This takes some flexibility from the modeling of the material functions but significantly reduces later optimization cost.

Kinematic hardening is modeled by the backstress tensor $\boldsymbol{X}$. Its evolution is defined in a phenomenological manner using ideas of Döring et al. [25], whose model bases on the work of Jiang and Sehitoglu [22]. The evolution is prescribed using the objective Oldroyd rate defined by

$$\overset{\triangledown}{\boldsymbol{X}} = \dot{\boldsymbol{X}} - \boldsymbol{l} \cdot \boldsymbol{X} - \boldsymbol{X} \cdot \boldsymbol{l}^{\mathrm{T}}\ . \tag{10}$$

With this definition at hand, the effective backstress tensor is decomposed in M individual backstresses

$$\overset{\triangledown}{\boldsymbol{X}} = \sum_{i=1}^{M} \overset{\triangledown}{\boldsymbol{X}}^{(i)} \tag{11}$$

[5] It seems worth mentioning that this is not the yield limit in uniaxial tension. Due to the formulation of Eq. 5, the uniaxial tensile yield stress max be computed via $\sigma_y = \sqrt{\frac{3}{2}}R$.

with[6]

$$\overset{\triangledown}{\boldsymbol{X}}{}^{(i)} = c^{(i)} \left[r^{(i)}\, \boldsymbol{n} - \left(\frac{||\boldsymbol{X}^{(i)}||_{\mathrm{F}}}{|r^{(i)}|} \right)^{Q^{(i)}} \boldsymbol{X}^{(i)} \right] \dot{p} + \frac{\boldsymbol{X}^{(i)}}{2\, r^{(i)}}\, \dot{r}^{(i)} \tag{12}$$

and the evolution of the material functions

$$\dot{r}^{(i)} = b \left(r_{\mathrm{T}}^{(i)} - r^{(i)} \right) \dot{p} \tag{13}$$

is described using the target functions [25]

$$r_{\mathrm{T}}^{(i)} = r_0^{(i)} \left[1 + \frac{a_1^{(i)}}{(1 + b_1\, p)^2} \right] . \tag{14}$$

Each backstress $\boldsymbol{X}^{(i)}$ requires the assignment of the additional material parameters $c^{(i)}$, $r_0^{(i)}$, $a_1^{(i)}$ and $Q^{(i)}$. As with isotropic hardening, only one transient term is considered in Eq. 14 compared to [25] in order to reduce model complexity. Since depending on the choice of $c^{(i)}$, a certain section of the monotonic stress–strain curve is described, several backstresses are required for a sufficiently smooth modeling of this. According to experience and [25], 5 backstresses, i.e., $i \in \{1, 2, 3, 4, 5\}$, should be used with the present model. The thermodynamic consistency of the model is discussed in A.

Isotropic and kinematic hardening both contain material functions in Eq. 8 and Eq. 13 dependent on p, which are defined as differential equations separately. This offers the possibility to chose initial values of the parameter functions R_{init} and $r_{\mathrm{init}}^{(i)}$ independently from the further function course. Especially the modeling of the initial material response and the initial stress–strain curve under monotonic loading can thus be improved. A higher-level material parameter b determines how fast the material functions asymptotically approach the target functions, respectively. The influence is depicted exemplary in the later Fig. 13.

The material model is implemented in ABAQUS/Standard [51] as UMAT user subroutine. Therefore, the time discretization of the plastic flow Eq. 6 is carried out using an exponential map backward integrator. It retains the form of a small-strain format algorithm when only small elastic strains are considered in the presence of kinematic hardening, see [54]. The evolution Eqs. 8 and 13 of the material functions are integrated using an Euler backward scheme. For the kinematic hardening relation in Eq. 12, the fully implicit objective integration of the Oldroyd rate is deployed. The solution procedure of the resulting nonlinear equation system is carried out using the successive substitution algorithm of Kobayashi and Ohno [56]. Finally, the overall predictor–corrector scheme is implemented in the user subroutine using *Mathematica* [57] in conjunction with the package *AceGen* [58,59].

3.4 Model parametrization

In order to provide a prediction of the residual stress evolution under cyclic loading in the bending specimen, a suitable parametrization of the outlined material model for 42CrMo4+QT is needed. All specimens used in the parametrization experiments conducted in the following were manufactured from the same material batch as the bending specimen from Sect. 2.1 using the same manufacturing process and parameters. All parametrization data used can be found in [43].

The determination of the material parameters introduced in Sect. 3.3 is a non-trivial task, as their coupling in the evolution equations makes it difficult to clearly separate the influences on material behavior in certain loading situations. A simple determination from a few tests, e.g., quasi-static tensile tests, is hardly possible. Rather, cyclic stress–strain paths must be considered in different variants in order to enable suitable predictions for the cyclic material behavior. In Döring et al. [25], inspired by Jiang and Sehitoglu [23], a generic way is presented, which yields most of the parameters in a straightforward manner without the application of an inverse parametrization algorithm. In a first step, we use this procedure in order to determine an initial set of parameters. However, some parameters are not determinable without the numerical application of the material

[6] In [25,26], the last term in Eq. 12 was introduced without the factor 1/2. Since we were unable to prove thermodynamic consistency for arbitrary loadings and parameters without the factor using the method of Appendix A, we included it in our model.

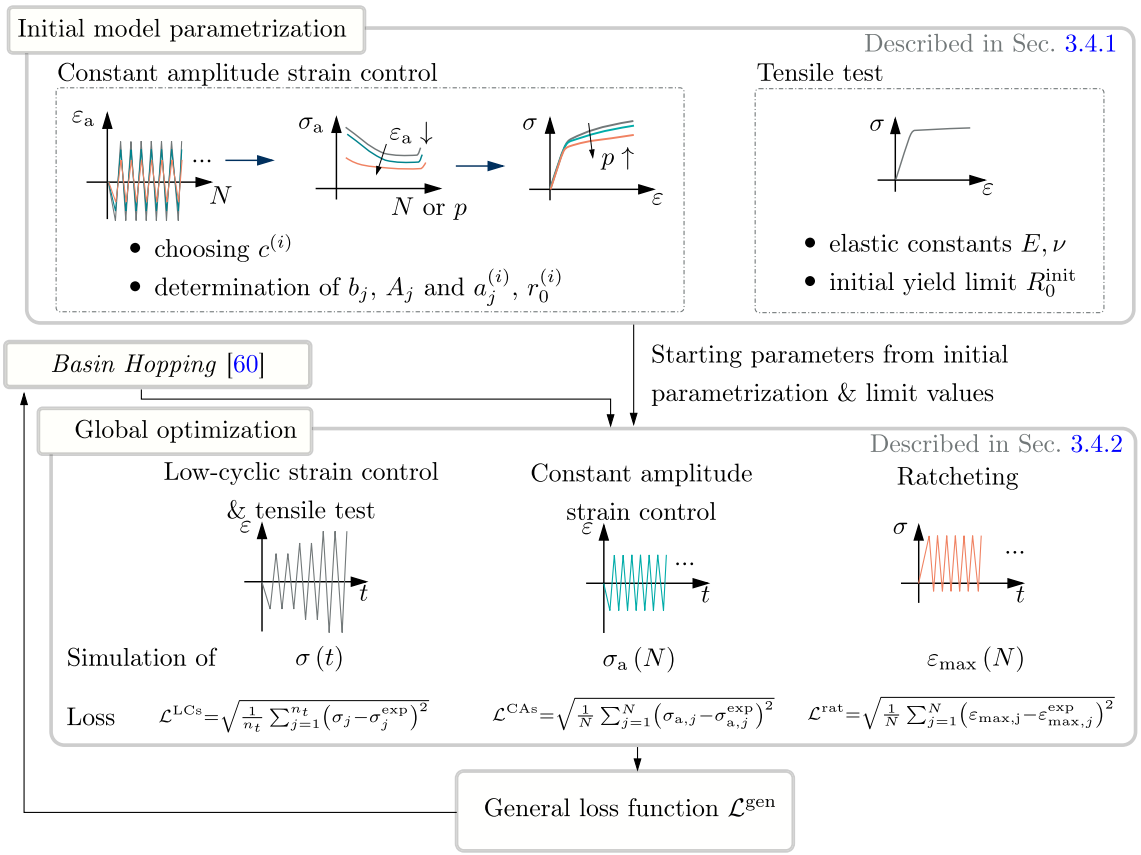

Fig. 10 Overall parametrization procedure consting of initial value determination and a global optimization scheme with the aim of minimizing the loss function. The procedure is implemented in *Python* using *Mathematica* and the package *AceGen*

Table 2 Material properties from the tensile test

E	ν	$R_{\text{p0.2}}$	R_{m}
204 401 MPa	0.253	1050 MPa	1133 MPa

model itself. Consequently, we use the initial parameter set as input for a subsequent global optimization scheme in Sect. 3.4.2 to improve the parametrization and to determine the remaining unknown parameters. The overall procedure is summarized in Fig. 10.

3.4.1 Initial model parametrization

For the initial parametrization, the elastic properties, the yield strength $R_{\text{p0.2}}$ as well as the tensile strength R_{m} are determined. They result from a tensile test following DIN EN ISO 6892-1 with a specimen geometry according to DIN 50125-E 8 × 8 × 46. For the evaluation, the DIC system ARAMIS is used. The results are summarized in Table 2.

In the next step, the material parameters mainly responsible for the cyclic transient behavior under symmetric strain-controlled loading are determined. For this purpose, strain-controlled constant amplitude fatigue tests with a load ratio $R_\sigma = -1$ using material specimens were carried out. The specimen geometry and the obtained results are depicted in Fig. 11. They indicate a cyclic softening behavior of the material. Closely following [25], one can construct stress–strain curves depending on N from Fig. 11b and transform them into a dependency on p. Hence, stress–strain curves for discrete p values are obtained. Equation 12 may then be reformulated for the uniaxial loading case, from which the values for $r^{(i)}$ and R can be calculated for each discrete stress–strain curve. Thereby, the parameter $c^{(i)}$ determines the plastic strain range on which the backstress i is active. Hence, the $c^{(i)}$ are chosen such that a smooth stress strain curve is achieved for the

Table 3 Initial values for further optimization based on a fit to constant strain amplitude data of a single specimen

(a) Isotropic hardening		
R_0/MPa	b_1	A_1
425.2	2.86	0.2
(b) Kinematic hardening		
$r_0^{(i)}$/MPa	$c^{(i)}$	$a_1^{(i)}$
56.4	816.5	0.17
70.4	326.6	0.14
93.9	163.3	0.09
184	40.8	0.04
377.9	8.2	0

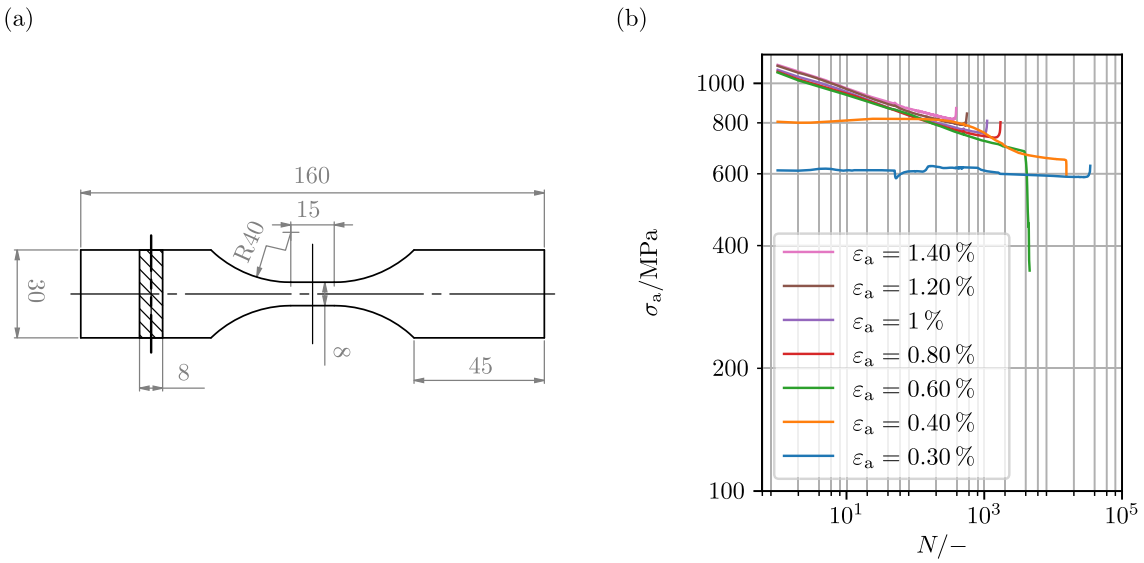

Fig. 11 Cyclic transient material behavior. **a** geometry of the specimen used throughout the whole cyclic characterization. Dimensions in mm. **b** experimental results from constant strain amplitude fatigue tests. The results are depicted until total specimen fracture

herein relevant strain ranges. Subsequently, the fit of material target functions $R_\mathrm{T}(p)$ and $r_\mathrm{T}^{(i)}(p)$ is carried out, yielding the corresponding parameters in Table 3[7]. Note that this is only the initial parametrization. Thus, for the sake of brevity, see [23,25] for more information on this parametrization procedure.

3.4.2 Global parameter optimization

A global optimization scheme is implemented using the initial parameters from Sect. 3.4.1 as start values. Additional experiments complement the tests already used for the initial parameterization and enable an inverse parameterization through the use of *Python* and a uniaxial implementation of the material model. The experimentally obtained $\sigma(t)$ or $\varepsilon(t)$ courses from the uniaxial tests are prescribed in the simulation, depending on the type of experiment. After the simulation, the difference between the simulated stress or strain curve and the experimental curve is used to formulate the loss function. In this way, an improved parameter set is achieved by applying an iterative minimization strategy. See Fig. 10 for the overall procedure.

The initial transient material behavior is accounted for by low-cycle uniaxial experiments under strain control. For this type of experiment, two variants are used in the following. The first is the monotonic tensile test,

[7] A single-parameter set could be determined for each material specimen, respectively, or for all specimens together using the discrete p data with the corresponding σ_a-ε_a values. It appears as Döring et al. [25] followed the latter approach. Since it was found that for the present material the single specimen procedure yields smoother parameter curves due to more data points for the regression of the stress–strain curves, it was used for the initial value determination. The data of the best-fitting parameter set were used for the subsequent optimization.

Table 4 Obtained material parameters from the parametrization algorithm and used settings for the optimization. The model parameter $b = 200$ was chosen in accordance with Döring et al. [25]

(a) Isotropic hardening

R_0/MPa	R_{init}/MPa	b	b_1	A_1
541.28	815.4	200	5.48	0.07

(b) Kinematic hardening

$r_0^{(i)}$/MPa	$r_{\text{init}}^{(i)}$/MPa	$c^{(i)}$	$Q^{(i)}$	$a_1^{(i)}$
58.7	50.46	816.5	1.5	0.06
43.7	17.71	326.6	1.5	0
111.2	184.61	163.3	2.13	−0.07
211.2	110.6	40.8	2.08	−0.08
188.9	179.39	8.2	5.76	0

(c) Parametrization settings

n_{it}	w_{LCs}	n_{LCs}	w_{CAs}	n_{CAs}	w_{rat}	n_{rat}
30	1	3	1	1	1.1	5

already used in Sect. 3.4.1. The latter denotes experiments with stepwise defined and continuously increasing strain amplitude, see Fig. 10. Several specimens were tested under these conditions and evaluated using the DIC system ARAMIS. For optimization, the root-mean-square error is calculated for the simulations with respect to the experimental data. Due to the swelling load acting on the bending beam, ratcheting occurs, which is underlined by Fig. 6. Accordingly, as depicted in Fig. 10, and in order to put special emphasis on this phenomenon, uniaxial ratcheting tests are carried out and used for the material model parametrization. Multiple load levels are considered and simulated during optimization. Again, the root-mean-square error is used and formulated for the maximum strain during each simulated load cycle. The third type of experiment considered for optimization are the constant strain amplitude tests already used in Sect. 3.4.1 and depicted in Fig. 11b. Their simulated and experimentally measured stress amplitude σ_{a} over fatigue life is used to formulate the loss function.

The three types of experiments are used for the formulation of the general loss function:

$$\mathcal{L}^{\text{gen}} = w_{\text{LCs}} \frac{\mathcal{L}^{\text{LCs}}}{n_{\text{LCs}}} + w_{\text{CAs}} \frac{\mathcal{L}^{\text{CAs}}}{n_{\text{CAs}}} + w_{\text{rat}} \frac{\mathcal{L}^{\text{rat}}}{n_{\text{rat}}} \,. \tag{15}$$

The loss is normalized by the number of simulated specimens n_{LCs}, n_{CAs} and n_{rat} and scaled by the weighting parameters w_{LCs}, w_{CAs} and w_{rat}, respectively. Several optimization runs with different settings were carried out whereby the global optimization algorithm Basin Hopping [60] was found to be the most promising global optimizer for the case at hand. For its application the parameter number of global iterations n_{it} needs to be chosen by the user. Each global iteration contains a local minimization procedure with the L-BFGS-B algorithm [61]. After the final global iteration is carried out, a last gradient-based local minimization is performed in order to further improve the result.

The result of the parameterized material model with respect to the experiments is depicted in Fig. 12 while the used parametrization settings and the resulting parameters are included in Table 4. The parametrization result yields a good accordance with the initial monotonic loading curve in Fig. 12. This is important since the absolute values of resulting residual stresses strongly depend on the initial loading curve. For subsequent loading, the behavior under cyclic loading gains relevance. The low-cyclic loading with increasing strain amplitude shows a good quantitative result, especially for the strain range from 0.5 % to 2 %, see Fig. 12b, which represents the relevant strain range for the cyclic bending under consideration, see Fig. 4c. Lastly, the result of the ratcheting simulations indicate a good agreement for multiple load levels, cf. Figure 12d. Slight deviations observed may be attributed to the diverse parametrization tests and some scatter in the experiments. The resulting material functions $R(p)$, $r^{(i)}(p)$ and their target functions are compared in Fig. 13. Starting from the found values for $r_{\text{init}}^{(i)}$ at $p = 0$ in Fig. 13b, one observes a pronounced evolution of $r_{\text{T}}^{(i)}$ for small p. Subsequent changes for larger p are comparably small and a stabilization level is reached. For parametrizing the case at hand, nearly constant $r_{\text{T}}^{(i)}$ can be observed. This indicates that the material can be described by constant material functions for the kinematic hardening in Eq. 12 right after the very initial transient behavior, i.e., $p > 1 \times 10^{-2}$. This does not hold true for the evolution of $R(p)$ in Fig. 13a. First, the same initial

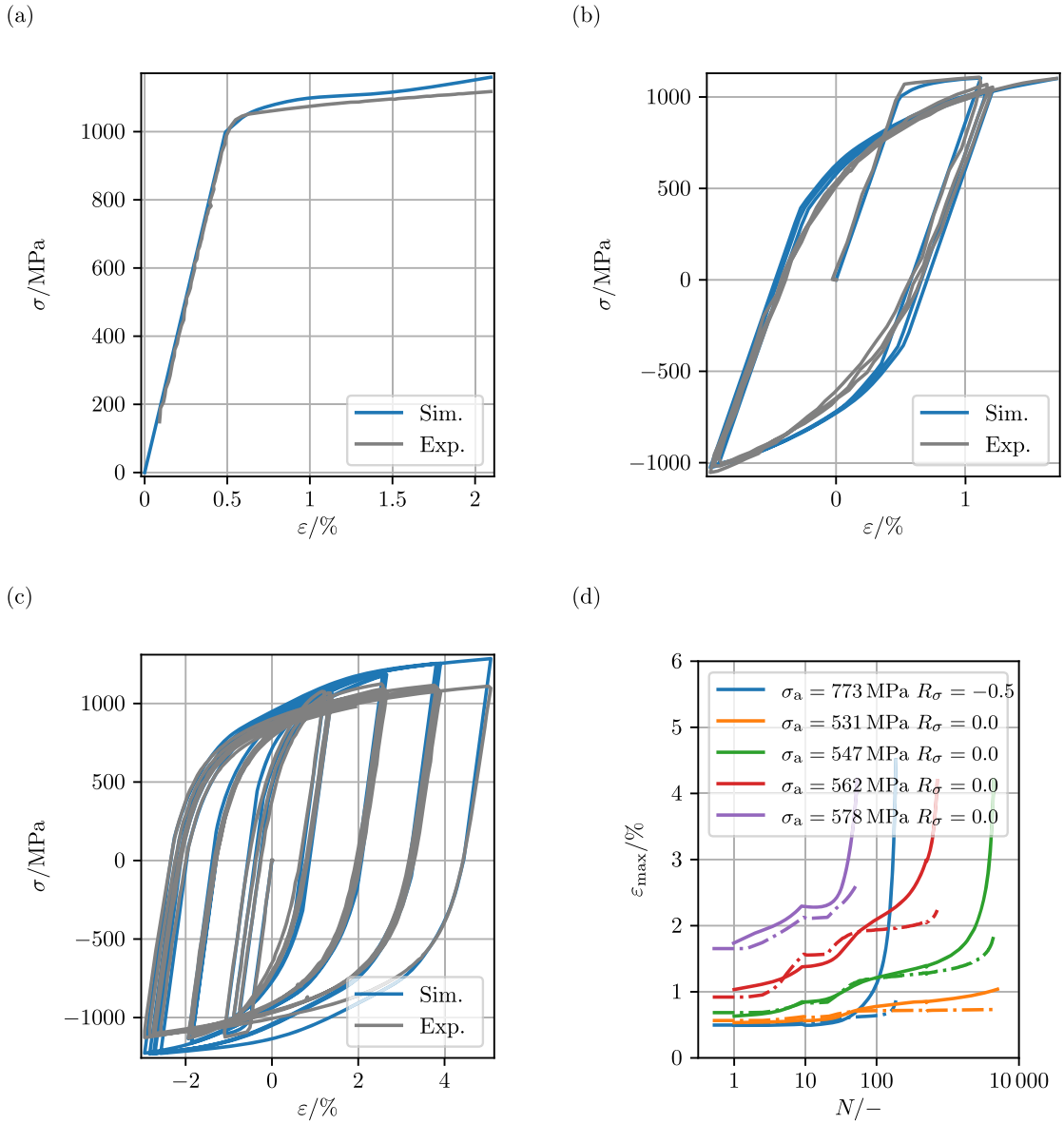

Fig. 12 Result of the material model parametrization using the proposed optimization scheme. For each type of loading, multiple single specimen data was used for the parametrization. Exemplary are shown here: **a**, **b** and **c** strain-controlled low-cyclic loading with experimental and simulative results. **d** result of ratcheting experiments (——) compared to the simulations (-·-·-)

asymptotic approach to the target function can be observed for $R\,(p)$. However, for increasing p even after the very initial behavior, a decrease in $R\,(p)$ is observed. This can be interpreted as cyclic softening, already indicated by Fig. 11b.

Overall, one has to admit that the simulation of several experiments with up to $N = 5000$ is a time intensive task leading to a necessary priorization in the choice of the parametrization settings. In conjunction with limited available computation time, this may result in a lack of generality of the procedure in terms of a real global minimum of the loss function. Additionally, the different experiments and the usual deviations for different specimen being tested leads to uncertainties, which is not accounted for in the parametrization. Nevertheless, the quality of the overall parametrization appears sufficient for the subsequent simulation of the bending experiments.

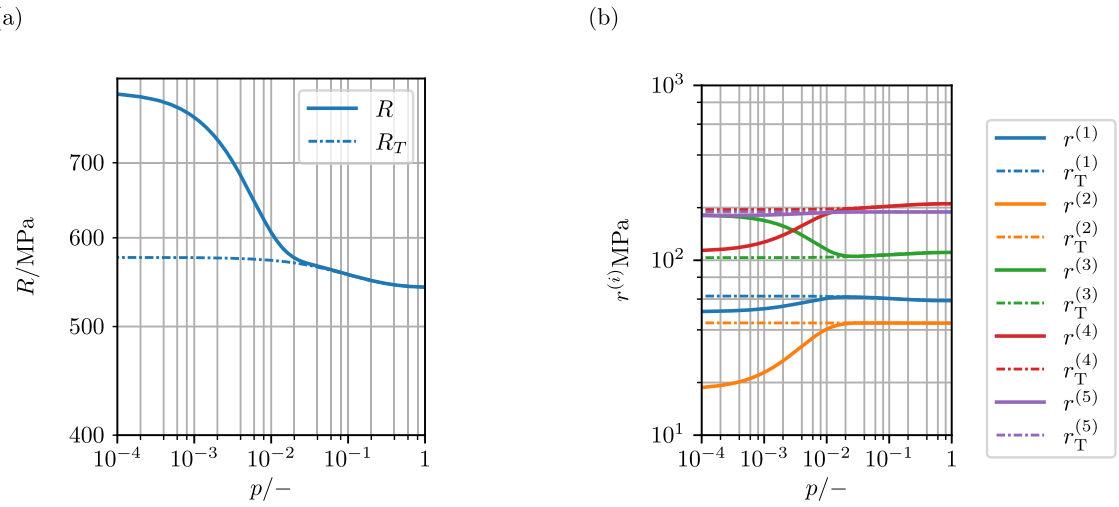

Fig. 13 Material functions and their targets. **a** isotropic hardening and **b** kinematic hardening. The curves correspond to the material parameters determined by the parametrization algorithm

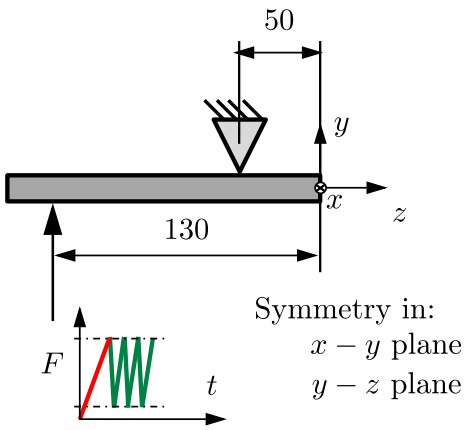

Fig. 14 Setup of the cyclic FE model for the simulations of residual stress evolution under cyclic loading. A quarter model with node-fixed boundary conditions is used. Dimensions in mm

4 Numerical results

In the next step, the experimental data gained in Sect. 2 and simulation results of the cyclic bending experiment using the proposed and parameterized material model from Sect. 3 are compared. The description of the residual stress evolution is followed by a discussion on the modeling of the initial load cycle. Afterward, general comments are made regarding the obtained numerical results.

4.1 Simulation of residual stress evolution

A FE model is set up for the simulation of the cyclic experiments from Sect. 2.5 using the parameterized material model from Sect. 3.3 in the commercial software ABAQUS/Standard [51]. Due to symmetry, the bending beam is modeled as a quarter model using 3D continuum elements with second-order ansatz functions. The mesh is chosen to be uniform over the domain of constant bending moment whereby 16 hexahedron elements were used over the beam's thickness. The boundary conditions are applied as node-fixed line-loads over the width of the beam and depicted in Fig. 14.

The load level is chosen as in the experiment. In order to determine the evolution of residual stresses from the model, multiple simulations are carried out. Each simulation considers a certain number of load cycles

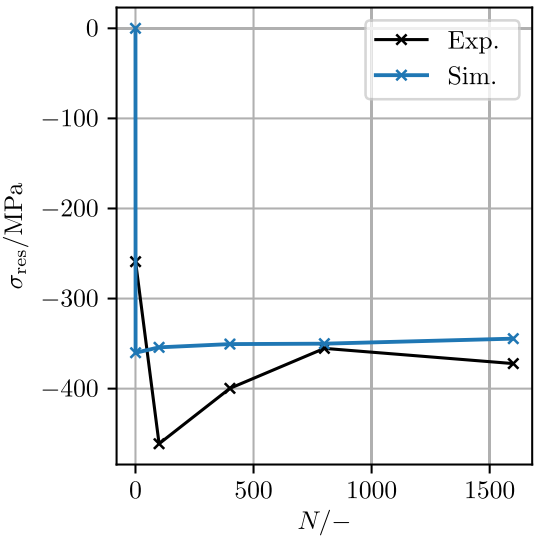

Fig. 15 Simulation results for the cyclic model. Depicted is the residual stress evolution at the surface of the bending specimen. The evaluation point is located in $x - y$ plane on the beam's tension side leading to compressive residual stresses

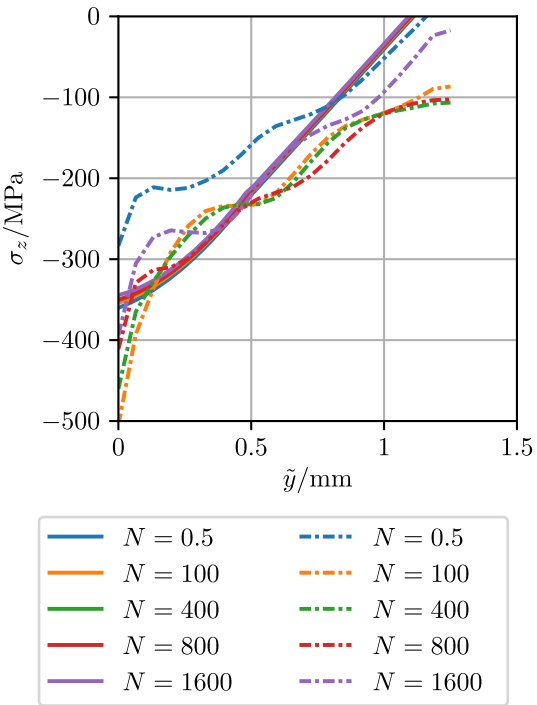

Fig. 16 Simulated residual stress profile (——) over the distance to the beam's tension side surface at various load cycles compared to the experimental ones (- · - ·)

after which the beam is unloaded, respectively. Therefore, the load cycles are simulated explicitly. It is ensured that the reversal points of each load cycle are considered correctly. The remaining stress after unloading is declared as simulated residual stress.

The residual stress at the surface of the beam is plotted over N in Fig. 15.

The comparison of the simulation results with the experimentally determined residual stresses on the surface generally shows a qualitative agreement of the functional curves. Initial loading of the beam induces an initial residual stress at $N = 0.5$. Subsequently, a slight relaxation is observed, leading to a decrease in the residual stress level and a stabilization phase. The simulations are carried out up to a maximum number of load cycles

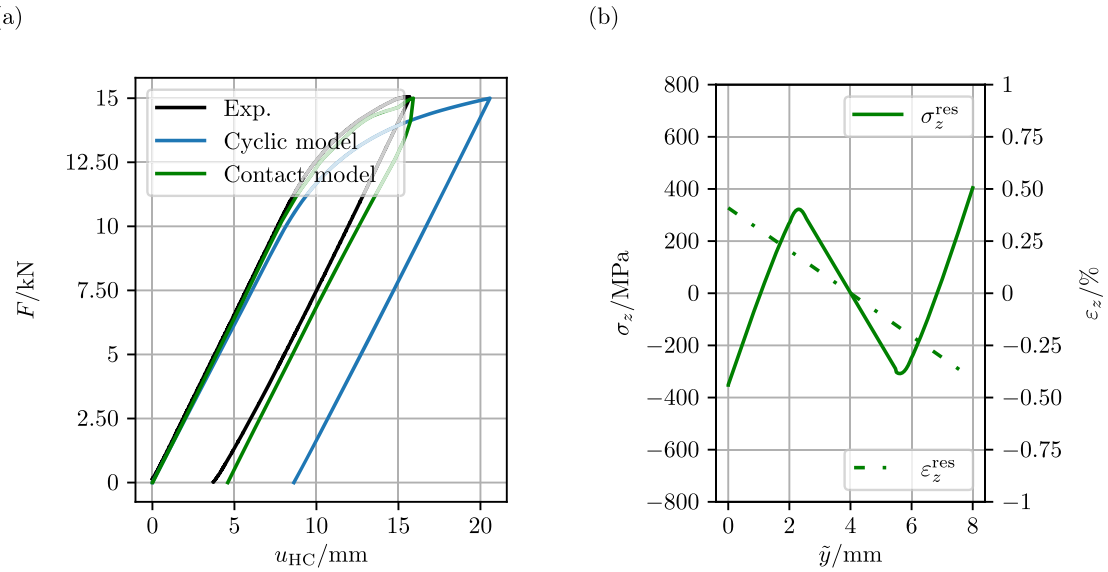

Fig. 17 Result of the simulation of the first load cycle. **a** the force–displacement curve of the hydraulic cylinder during the initial load cycle for experiment and the two different boundary conditions and **b** the residual stress and residual strain after the initial loading at $N = 0.5$ using the contact model

of $N_{\max} = 1.6 \times 10^3$. Due to the computational effort involving approx. 4 d using 8 CPUs, it is not possible to consider more load cycles while maintaining reasonable runtimes. Quantitatively, the residual stresses stabilize at a level consistent with the experimental results. However, there are deviations in the amount of residual stress change in early stages of fatigue life between experiment and simulation. The simulations show less pronounced residual stress evolution compared to the experimental findings, see Fig. 15 for $N < 500$. Similar results are found for the simulated residual stress profiles, which are plotted over the beam thickness and for different load cycle numbers in Fig. 16. Mainly, the stresses close to the surface are influenced by the cyclic loading, while the overall profile in total remains almost unchanged, valid for both simulation and experiment. In comparison of simulation and experiment a different slope of the residual stress profiles is found directly at the surface, for $\tilde{y} \to 0$ in Fig. 16.

A possible reason for the discrepancies between simulation and experiment may be the material's microstructure, which influences residual stress formation and evolution, especially at small length scales, but is not taken into account in the present macroscopic model. Beltrami et al. [62] showed, for the example of additively manufactured stainless steel, that the microstructure has significant influence of the resulting residual stress evolution under cyclic loading. Differences in the near-surface slope of the profile shown in Fig. 16 can be influenced by the experimental analysis method used, the incremental hole drilling method, which has the greatest uncertainties directly at the surface. Additionally, a good overall stability of the residual stresses is observed for the investigated loading case, which is in line with the high yield strength of the high-strength steel, offering a large range of purely elastic deformation. This could also explain the low residual stress evolution observed in the simulation. General comments in this regard are provided in the later Sect. 4.3.

4.2 Simulation of the first load cycle

Using the same model as in Sect. 4.1, further results may be discussed with respect to Fig. 17a, in which the simulated deflection of the beam's support structure is compared to the experimentally determined deflection curve for the first load cycle. For comparison, the model from Sect. 4.1 is referred to as cyclic model. Obviously, for the cyclic model, the simulated deflection does not match the experimental one and is predicted to be too high. The reason for this is to be found in the simplified boundary conditions of the simulation. Given the real geometry of the support structures and the fact that they allow slight beam sliding, a better prediction would require modeling that takes into account the complex kinematics, i.e., the actual frictional contact of the beam with the supports.

In order to prove this assumption, a contact model is set up. The only difference to the cyclic model are the prescribed boundary conditions. The supports are modeled as rigid body cylinders, and the contact is discretized with ABAQUS surface-to-surface contact pairs [63] using Coulomb's friction model. The constant friction coefficient is assumed as steel-steel contact typical to $\mu_0 = 0.15$ [64]. A simulation of the first load cycle is carried out. When comparing the displacement of the beam support structures depicted in Fig. 17a, the same amount of deflection is found in both experiment and simulation for the contact model. This also applies to the resulting strain profile from the simulation and the experiment, cf. Figures 4c and 17b. The prediction of the residual stress after initial loading is also improved. While from the experiment $\sigma_z^{\mathrm{res}} = -290\,\mathrm{MPa}$ is determined at the tension side of the beam, $\approx -360\,\mathrm{MPa}$ results from the simulation at the same evaluation point. This discrepancy may be explained again by the uncertainty of the experimental residual stress analysis in layers close to the surface when deploying the incremental hole drilling method, which is mainly due to microstructure inhomogeneities which are not considered in the simulations. Furthermore, a better prediction could be achieved with additional experimental data regarding the contact properties. The same holds true for Fig. 5b observed rotations of the support structures in the experiment, which could be modeled with additional torsional springs between the supports and the ground. However, such a more detailed modeling of the initial loading is beyond the scope of this paper.

Although it provides good results for the first load cycle, the modeling of the frictional contact is not considered useful for the simulation of cyclic loading and is therefore not dealt with here. The reason for this, in addition to the enormous computing times that would result and the generally decreasing robustness of the simulation, is the contact stabilization. Pre-tests showed that an activated numerical stabilization leads to an unknown and accumulating influence of numerical damping over fatigue life. Disabling the stabilization makes the simulation unstable and non-convergent. Nevertheless, since this only occurred during cyclic loading, the initial load cycle can be simulated using the contact formulation.

4.3 General remarks on the numerical results

As a result of the investigation using the proposed modeling strategy to simulate the combined residual stress generation and evolution under cyclic loading within a single model, and with respect to the numerical results of Sects. 4.1 and 4.2, the following statements are made. First, the presented model can consider multiple thousands of load cycles explicitly in computational times of approx. 4 d using 8 CPUs on a high performance cluster. Despite an already quite complex material model, achieving more accurate quantitative statements and improved predictions would require a more complex modeling approach leading to larger models, e.g., to account for complex boundary conditions or to consider damage and microstructure. This, in turn, would demand exponentially increasing computational efforts for both parameterization and validation. Second, for the special case at hand, the simulation of residual stress evolution during cyclic loading is possible in principle using cyclic plasticity models. For cyclic bending, the stabilization level of residual stress can be predicted after approximately two thousand load cycles, and an improved prediction for the first load cycle can be achieved if the actual contact between the beam and the supports is considered in the model. However, in the presented setup, the experimentally determined change of residual stresses under the cyclic loading was quite low which was already attributed to the large yield strength, cf. Figure 12a and Table 2, and therefore good residual stress stability for the case at hand. As a result, the simulation only shows small changes in residual stress, since the used macroscopic yield stress of the model is only slightly exceeded. Better simulative predictions may be possible when considering higher load levels with more pronounced residual stress evolution or a different material [39]. Since increasing load would exponentially decrease the fatigue life of the specimens, this was not intended here. Finally, it seems worth noting that the nevertheless relatively high load level and the fact, that no reverse loading was considered, hardly allow any conclusions on the general stability of the residual stresses under arbitrary conditions. Such statements would always be tied to a specific test setup and a specific load level, as the change in residual stress is very sensitive in this respect due to its local character, which is caused by the strong inhomogeneity of residual stress profiles.

5 Conclusion

In the present manuscript, an experimental and numerical approach for the investigation of the residual stress evolution under cyclic mechanical loading is presented. In the 4-point bending test, specimens are loaded

cyclically in the tensile swelling regime. The bending specimens subsequently undergo experimental residual stress analysis on the tension side using the incremental hole drilling method in order to investigate the residual stress evolution during the cyclic loading. The results for the load case under consideration show an initial phase of residual stress change followed by a stabilization phase, after which the residual stress change is comparatively small. The results obtained are used for comparison with a numerical prediction using a cyclic plasticity model that accounts for the large deflections with a parameterization using uniaxial material data. For predicting the cyclic change of residual stresses, a FE model accounting for the symmetry of the setup is deployed. The simulated residual stress evolution over the accumulating load cycle number matches the experimental results qualitatively. The stabilization level of residual stresses after approximately two thousand load cycles can be predicted in principle, making the approach particularly suitable for low-cycle fatigue. Improving prediction for the initial load cycle is achieved by incorporating frictional contact modeling between the beam and its supports. The high-strength steel under consideration shows only moderate change of residual stress under cyclic loading, which is also apparent in the simulation.

The investigation shows that the simulation of the combined formation and evolution of residual stresses with a single model is a non-trivial task. While the simulation of the initial loading can be carried out with reasonable effort, the cyclic prediction is coupled to a certain computational and temporal expense. This arises from two issues: First, to capture the cyclic transient material behavior, a cyclic plasticity model is needed, which in turn requires a suitable and costly parametrization. Second, during simulation, an extensive parallelization of the FE model on a high-performance cluster is only useful to a limited extent, since the main cost results from the huge number of increments to simulate. In addition, due to the highly inhomogeneous residual stress profiles, the consideration of the microstructure appears necessary for an improved prediction, which in turn influences the required computing power and time. This issues need to be addressed in future work. The approach of two-stage modeling, as pursued for example in [37,38], with a process model for the generation of residual stresses and a separate and perhaps less complex material model for the cyclic loading appears to be an alternative in this context.

Acknowledgements This contribution results from a collaboration supported by the Deutsche Forschungsgemeinschaft (DFG) in the Priority Program SPP2013 - Targeted Use of Forming Induced Residual Stresses in Metal Components with Grant No. KA 3309/7-3 and Grant No. KA 3309/21-1. Thanks go to the scientific staff at the IAM-WK who participated in the time-consuming hole drilling analyses, in particular Dhruvit Gabani, Florian Lang and Nicola Simon. We also thank the members of the expert group *Simulation and Modelling* of SPP2013 for the discussions from which the present paper results. Jörg Brummund's support in the discussions on continuum mechanics is greatly appreciated. We are grateful to the Zentrum für Informationsdienste und Hochleistungsrechnen (ZIH) at TU Dresden for providing its facilities for high-performance calculations.

Author contribution T.S.: Conceptualization, Formal Analysis, Investigation, Methodology, Visualization, Software, Writing - original draft, Writing - review & editing J.G.: Formal Analysis, Investigation, Methodology, Resources, Writing - original draft, Writing - review & editing M.K.: Conceptualization, Funding acquisition, Project administration, Resources, Supervision, Writing - review & editing.

Funding Open Access funding enabled and organized by Projekt DEAL.

Data availability The experimental data used here is freely available in Schneider et al. - Experimental analysis of residual stress evolution under cyclic mechanical loading in 42CrMo4+QT (1.7225) including parametrization data. OpARA - Open Access Repository and Archive (2024). https://doi.org/10.25532/OPARA-288.

Declarations

Conflict of interest The authors declare no competing interests.

Appendix A Proof of consistency for small strains

For infinitesimal strain $\boldsymbol{\varepsilon}$, we want to proof thermodynamic consistency of the model elements from the present paper. For this purpose, the same kinematic hardening rule as in the main part of the paper, which is the most critical part of the plasticity model regarding proof of consistency, is applied. A general form of isotropic hardening is considered, which includes the special case used in this work. The model under consideration relies on the additive split of strain

$$\boldsymbol{\varepsilon} = \boldsymbol{\varepsilon}^{\mathrm{e}} + \boldsymbol{\varepsilon}^{\mathrm{p}} \,, \tag{A1}$$

into elastic and plastic parts, the normality flow rule

$$\dot{\boldsymbol{\varepsilon}}^{\mathrm{p}} = \dot{p} \, \underbrace{\frac{\partial f}{\partial \boldsymbol{\sigma}}}_{\boldsymbol{n}} \,, \tag{A2}$$

and the kinematic hardening rule to be proofed for consistency

$$\dot{\boldsymbol{X}}^{(i)} = c^{(i)} \left[r^{(i)} \, \boldsymbol{n} - \left(\frac{||\boldsymbol{X}^{(i)}||_{\mathrm{F}}}{|r^{(i)}|} \right)^{Q^{(i)}} \boldsymbol{X}^{(i)} \right] \dot{p} + \frac{\boldsymbol{X}^{(i)}}{2 r^{(i)}} \, \dot{r}^{(i)} \,. \tag{A3}$$

The yield function

$$f = ||\boldsymbol{s} - \boldsymbol{X}||_{\mathrm{F}} - \tilde{R} \,, \tag{A4}$$

and the KKT conditions

$$\dot{p} \geq 0, \; f \leq 0, \; \dot{p} \, f = 0 \tag{A5}$$

are employed. An ansatz for the backstress

$$\boldsymbol{X}^{(i)} := h^{(i)} \left[\boldsymbol{\varepsilon}^{\mathrm{p}} - \boldsymbol{\xi}^{(i)} \right] \tag{A6}$$

and the general isotropic hardening with its initial value $\tilde{R}_{\mathrm{init}}$

$$\tilde{R} := \tilde{R}_{\mathrm{init}} + g \tag{A7}$$

is defined. Therein, we introduce the strain-like internal variables $\boldsymbol{\xi}^{(i)}$ for kinematic hardening and a stress-like variable g for isotropic hardening. For the case at hand, one may formulate the free energy density

$$\psi \left(\boldsymbol{\varepsilon}^{\mathrm{e}}, \, \boldsymbol{\varepsilon}^{\mathrm{p}}, \, p, \, \boldsymbol{\xi}^{(i)} \right) = \psi^{\mathrm{e}} \left(\boldsymbol{\varepsilon}^{\mathrm{e}} \right) + \int_0^p g \left(\tilde{p} \right) \mathrm{d}\tilde{p} + \sum_{i=1}^{N} \frac{1}{2} h^{(i)} \left(r^{(i)} \left(p \right) \right) \, ||\boldsymbol{\varepsilon}^{\mathrm{p}} - \boldsymbol{\xi}^{(i)}||_{\mathrm{F}}^2 \,, \tag{A8}$$

wherein $h^{(i)}$ are scalar functions that are implicitly derived from p via the material functions $r^{(i)} \left(p \right) \geq 0$. To ensure thermodynamic consistency under isothermal conditions, the model must meet the following Clausius–Duhem inequality

$$\boldsymbol{\sigma} : \dot{\boldsymbol{\varepsilon}} - \dot{\psi} \geq 0 \,. \tag{A9}$$

Inserting the derivatives leads to

$$\boldsymbol{\sigma} : \left(\dot{\boldsymbol{\varepsilon}}^{\mathrm{e}} + \dot{\boldsymbol{\varepsilon}}^{\mathrm{p}} \right) - \frac{\partial \psi^{\mathrm{e}}}{\partial \boldsymbol{\varepsilon}^{\mathrm{e}}} \, \dot{\boldsymbol{\varepsilon}}^{\mathrm{e}} - g \, \dot{p} - \sum_{i=1}^{N} h^{(i)} \left(\boldsymbol{\varepsilon}^{\mathrm{p}} - \boldsymbol{\xi}^{(i)} \right) : \left(\dot{\boldsymbol{\varepsilon}}^{\mathrm{p}} - \dot{\boldsymbol{\xi}}^{(i)} \right) - \sum_{i=1}^{N} \frac{||\boldsymbol{\varepsilon}^{\mathrm{p}} - \boldsymbol{\xi}^{(i)}||_{\mathrm{F}}^2}{2} \frac{\mathrm{d}h^{(i)}}{\mathrm{d}r^{(i)}} \, \dot{r}^{(i)} \geq 0 \,, \tag{A10}$$

from which the definition of the stress

$$\boldsymbol{\sigma} = \frac{\partial \psi^{\mathrm{e}}}{\partial \boldsymbol{\varepsilon}^{\mathrm{e}}} \tag{A11}$$

directly follows. Equation A4, Ineq. A5 and the flow rule from Eq. A2 are used to provide the identity

$$\boldsymbol{\sigma} : \dot{\boldsymbol{\varepsilon}}^{\mathrm{p}} - g \, \dot{p} = \tilde{R}_{\mathrm{init}} \, \dot{p} + \boldsymbol{X} : \dot{\boldsymbol{\varepsilon}}^{\mathrm{p}} \,. \tag{A12}$$

With the definitions at hand, Eq. A10 is rewritten as

$$\tilde{R}_{\mathrm{init}} \, \dot{p} + \boldsymbol{X} : \dot{\boldsymbol{\varepsilon}}^{\mathrm{p}} - \sum_{i=1}^{N} h^{(i)} \left(\boldsymbol{\varepsilon}^{\mathrm{p}} - \boldsymbol{\xi}^{(i)} \right) : \left(\dot{\boldsymbol{\varepsilon}}^{\mathrm{p}} - \dot{\boldsymbol{\xi}}^{(i)} \right) - \sum_{i=1}^{N} \frac{||\boldsymbol{\varepsilon}^{\mathrm{p}} - \boldsymbol{\xi}^{(i)}||_{\mathrm{F}}^2}{2} \frac{\mathrm{d}h^{(i)}}{\mathrm{d}r^{(i)}} \dot{r}^{(i)} \geq 0 \,. \tag{A13}$$

Taking Eq. A6 and its time derivative

$$\dot{\boldsymbol{\varepsilon}}^{\mathrm{p}} - \dot{\boldsymbol{\xi}}^{(i)} = \frac{1}{h^{(i)}} \left[\dot{\boldsymbol{X}}^{(i)} - \boldsymbol{X}^{(i)} \frac{\mathrm{d}h^{(i)}}{\mathrm{d}r^{(i)}} \frac{\dot{r}^{(i)}}{h^{(i)}} \right] \tag{A14}$$

into account and inserting them into Eq. A13 yields a general possibility to prove the consistency via

$$\underbrace{\tilde{R}_{\mathrm{init}}\,\dot{p}}_{\text{(A)}} + \sum_{i=1}^{N} \underbrace{\frac{\boldsymbol{X}^{(i)}}{h^{(i)}}\left[h^{(i)}\,\dot{\boldsymbol{\varepsilon}}^{\mathrm{p}} - \dot{\boldsymbol{X}}^{(i)} + \frac{1}{2}\frac{\boldsymbol{X}^{(i)}}{h^{(i)}}\frac{\mathrm{d}h^{(i)}}{\mathrm{d}r^{(i)}}\,\dot{r}^{(i)}\right]}_{\text{(B)}} \geq 0\ . \tag{A15}$$

It is (A) ≥ 0, since Ineq. A5 applies and $\tilde{R}_{\mathrm{init}} > 0$ is chosen in a physically meaningful way. Finally, the requirement of (B) ≥ 0 leads to a general form of the consistent evolution equation

$$\dot{\boldsymbol{X}}^{(i)} = h^{(i)}\,\dot{\boldsymbol{\varepsilon}}^{\mathrm{p}} + \frac{1}{2}\frac{\boldsymbol{X}^{(i)}}{h^{(i)}}\frac{\mathrm{d}h^{(i)}}{\mathrm{d}r^{(i)}}\,\dot{r}^{(i)} - f^{(i)}\left(\boldsymbol{X}^{(i)},\, r^{(i)}\right)\boldsymbol{X}^{(i)}\,\dot{p} \tag{A16}$$

with $f^{(i)}$ being additional positive scalar functions. Choosing $h^{(i)} = c^{(i)}\,r^{(i)}$ with $c^{(i)} > 0$ and

$$f^{(i)} = c^{(i)}\left(\frac{||\boldsymbol{X}^{(i)}||_{\mathrm{F}}}{|r^{(i)}|}\right)^{Q^{(i)}} \tag{A17}$$

yields the proposed evolution equation

$$\dot{\boldsymbol{X}}^{(i)} = c^{(i)}\left[r^{(i)}\,\boldsymbol{n} - \left(\frac{||\boldsymbol{X}^{(i)}||_{\mathrm{F}}}{|r^{(i)}|}\right)^{Q^{(i)}}\boldsymbol{X}^{(i)}\right]\dot{p} + \frac{\boldsymbol{X}^{(i)}}{2\,r^{(i)}}\,\dot{r}^{(i)}\ . \tag{A18}$$

References

1. Kästner, M., Volk, W.: Forming-induced residual stresses: experiment, modeling, simulation. Arch. Appl. Mech. **91**(8), 3463–3464 (2021). https://doi.org/10.1007/s00419-021-02007-y
2. Volk, W., Vogt, S., Stahl, J., Prauser, S.: Introduction to residual stresses in production technology. Prod. Eng. Res. Devel. **13**(2), 119–121 (2019). https://doi.org/10.1007/s11740-019-00881-8
3. Withers, P.J.: Residual stress and its role in failure. Rep. Prog. Phys. **70**(12), 2211–2264 (2007). https://doi.org/10.1088/0034-4885/70/12/R04
4. Macherauch, E., Wohlfahrt, H., Wolfstieg, U.: Zur zweckmäßigen Definition von Eigenspannungen. HTM J. Heat Treatment Mater. **28**(3), 201–211 (1973). https://doi.org/10.1515/htm-1973-280305
5. Kloos, K.H.: Eigenspannungen. Definition und Entstehungsursachen. Materialwissenschaft Werkst **10**(9), 293–302 (1979). https://doi.org/10.1002/mawe.19790100906
6. Hauk, V.M.: Evaluation of macro- and micro-residual stresses on textdeed materials by x-ray, neutron diffraction and defection measurements. Adv. X-ray Anal. **29**, 1–15 (1985). https://doi.org/10.1154/S0376030800010053
7. Hauk, V., Behnken, H.: Structural and Residual Stress Analysis by Nondestructive Methods: Evaluation, Application Assessment. Elsevier, Amsterdam (1997)
8. Macherauch, E.: Recent investigations on the development of residual stresses and their effect in metallic materials. Materialwissenschaft Werkst **10**(3), 97–111 (1979). https://doi.org/10.1002/mawe.19790100309
9. Macherauch, E., Kloos, K.H.: Bewertung von Eigenspannungen bei quasistatischer und schwingender Werkstoffbeanspruchung – Teil III. Materialwissenschaft Werkst **20**(3), 82–91 (1989). https://doi.org/10.1002/mawe.19890200313
10. Radaj, D., Vormwald, M.: Ermüdungsfestigkeit: Grundlagen Für Ingenieure, 3., neubearbeitete und erweiterte auflage edn. Springer, Berlin (2007). OCLC: 255665882
11. Haibach, E.: Betriebsfestigkeit: Verfahren und Daten zur Bauteilberechnung. Springer, Berlin; Heidelberg; New York (2006). OCLC: 873375834
12. Kühne, D., Spak, B., Kästner, M., Brosius, A., Fiedler, M.: Consideration of cyclic hardening and residual stresses in fatigue life calculations with the local strain approach. Arch. Appl. Mech. **91**(8), 3693–3707 (2021). https://doi.org/10.1007/s00419-021-01950-0
13. Guilleaume, C., Brosius, A.: Cross-rolling process for manufacturing lightweight hybrid components. Journal of Advanced Joining Processes 3, 100063 (2021) https://doi.org/10.1016/j.jajp.2021.100063
14. Seiler, M., Keller, S., Kashaev, N., Klusemann, B., Kästner, M.: Phase-field modelling for fatigue crack growth under laser shock peening-induced residual stresses. Arch. Appl. Mech. (2021). https://doi.org/10.1007/s00419-021-01897-2
15. Dawson, R., Moffat, D.G.: Vibratory stress relief: a fundamental study of its effectiveness. J. Eng. Mater. Technol. **102**(2), 169–176 (1980). https://doi.org/10.1115/1.3224793
16. Varvani-Farahani, A.: Nonlinear kinematic hardening cyclic plasticity. In: Cyclic Plasticity of Metals, pp. 139–174. Elsevier (2022). https://doi.org/10.1016/B978-0-12-819293-1.00015-2. https://linkinghub.elsevier.com/retrieve/pii/B9780128192931000152
17. Chaboche, J.L., Dang Van, K., Cordier, G.: Modelization of the Strain Memory Effect on the Cyclic Hardening of 316 Stainless Steel. North-Holland Publishing Co, Netherlands (1979). http://inis.iaea.org/search/search.aspx?orig_q=RN:12591218
18. Chaboche, J.L., Rousselier, G.: On the plastic and viscoplastic constitutive equations—part i: rules developed with internal variable concept. J. Pressure Vessel Technol. **105**(2), 153–158 (1983). https://doi.org/10.1115/1.3264257

19. Armstrong, P.J., Frederick, C.O.: A mathematical representation of the multiaxial Bauschinger effect. CEGB Report RD/B/N **731** (1966) https://doi.org/10.3184/096034007X207589
20. Ohno, N., Wang, J.-D.: Kinematic hardening rules with critical state of dynamic recovery, part I: formulation and basic features for ratchetting behavior. Int. J. Plast **9**(3), 375–390 (1993). https://doi.org/10.1016/0749-6419(93)90042-O
21. Ohno, N., Wang, J.-D.: Kinematic hardening rules with critical state of dynamic recovery, part II: Application to experiments of ratchetting behavior. Int. J. Plast **9**(3), 391–403 (1993). https://doi.org/10.1016/0749-6419(93)90043-P
22. Jiang, Y., Sehitoglu, H.: Modeling of cyclic ratchetting plasticity, part I: development of constitutive relations. J. Appl. Mech. **63**(3), 720–725 (1996). https://doi.org/10.1115/1.2823355
23. Jiang, Y., Sehitoglu, H.: Modeling of cyclic ratchetting plasticity, part II: comparison of model simulations with experiments. J. Appl. Mech. **63**(3), 726–733 (1996). https://doi.org/10.1115/1.2823356
24. Abdel-Karim, M., Ohno, N.: Kinematic hardening model suitable for ratchetting with steady-state. Int. J. Plast **16**(3–4), 225–240 (2000). https://doi.org/10.1016/S0749-6419(99)00052-2
25. Döring, R., Hoffmeyer, J., Seeger, T., Vormwald, M.: A plasticity model for calculating stress–strain sequences under multiaxial nonproportional cyclic loading. Comput. Mater. Sci. **28**(3–4), 587–596 (2003). https://doi.org/10.1016/j.commatsci.2003.08.015
26. Döring, R.: Zum Deformations- und Schädigungsverhalten matallischer Werkstoffe unter mehrachsig nichtproportionalen zyklischen Beanspruchungen. PhD thesis, Technische Universität Darmstadt, Darmstadt (2006)
27. Jahed, H., Roostaei, A. (eds.): Cyclic Plasticity of Metals: Modeling Fundamentals and Applications, 1st edn. Elsevier, San Diego (2022)
28. Chaboche, J.L.: A review of some plasticity and viscoplasticity constitutive theories. Int. J. Plast **24**(10), 1642–1693 (2008). https://doi.org/10.1016/j.ijplas.2008.03.009
29. Franceschi, A., Stahl, J., Kock, C., Selbmann, R., Ortmann-Ishkina, S., Jobst, A., Merklein, M., Kuhfuß, B., Bergmann, M., Behrens, B.-A., Volk, W., Groche, P.: Strategies for residual stress adjustment in bulk metal forming. Arch. Appl. Mech. **91**(8), 3557–3577 (2021). https://doi.org/10.1007/s00419-021-01903-7
30. Franceschi, A., Jaeger, F., Hoche, H., Oechsner, M., Groche, P.: Calibration of the residual stresses with an active die during the ejection phase of cold extrusion. Int. J. Mater. Form. **14**(2), 223–233 (2021). https://doi.org/10.1007/s12289-020-01572-x
31. Maaß, F., Hahn, M., Tekkaya, A.E.: Setting Residual Stresses in Tensile Stress-Superposed Incremental Sheet Forming. KEM 926, 655–662 (2022) https://doi.org/10.4028/p-232uip
32. Kajal, G., Tyagi, M.R., Kumar, G.: A review on the effect of residual stresses in incremental sheet metal forming used in automotive and medical sectors. Materials Today: Proceedings 78, 524–534 (2023) https://doi.org/10.1016/j.matpr.2022.11.235
33. Simon, N., Erdle, H., Walzer, S., Gibmeier, J., Böhlke, T., Liewald, M.: Residual stresses in deep-drawn cups made of duplex stainless steel X2CrNiN23-4: Influence of the drawing depth. Forsch. Ingenieurwes. **85**(3), 795–806 (2021). https://doi.org/10.1007/s10010-021-00497-4
34. Behrens, B.-A., Schröder, J., Brands, D., Scheunemann, L., Niekamp, R., Chugreev, A., Sarhil, M., Uebing, S., Kock, C.: Experimental and Numerical Investigations of the Development of Residual Stresses in Thermo-Mechanically Processed Cr-Alloyed Steel 1.3505. Metals 9(4), 480 (2019) https://doi.org/10.3390/met9040480
35. Uebing, S., Brands, D., Scheunemann, L., Schröder, J.: Residual stresses in hot bulk formed parts: two-scale approach for austenite-to-martensite phase transformation. Arch. Appl. Mech. **91**(2), 545–562 (2021). https://doi.org/10.1007/s00419-020-01836-7
36. Salvati, E., Korsunsky, A.M.: An analysis of macro- and micro-scale residual stresses of Type I, II and III using FIB-DIC micro-ring-core milling and crystal plasticity FE modelling. International Journal of Plasticity 98, 123–138 (2017) https://doi.org/10.1016/j.ijplas.2017.07.004
37. Dureau, C., Arzaghi, M., Grosdidier, T., Massion, R., Nadot, Y.: Modeling of the fatigue behavior of functionally graded materials: Study of the residual stresses induced by surface severe plastic deformation. Fatigue Fract Eng Mat Struct, 14221 (2023) https://doi.org/10.1111/ffe.14221
38. Franceschi, A., Kaffenberger, M., Schork, B., Hoche, H., Oechsner, M., Groche, P.: Observations on the stability of the residual stresses after cold forming and unidirectional loading. Prod. Eng. Res. Devel. **13**(2), 157–167 (2019). https://doi.org/10.1007/s11740-018-00871-2
39. McCLUNG, R.C.: A literature survey on the stability and significance of residual stresses during fatigue. Fat Frac Eng Mat Struct **30**(3), 173–205 (2007). https://doi.org/10.1111/j.1460-2695.2007.01102.x
40. Xie, X.-F., Jiang, W., Luo, Y., Xu, S., Gong, J.-M., Tu, S.-T.: A model to predict the relaxation of weld residual stress by cyclic load: experimental and finite element modeling. Int. J. Fat. **95**, 293–301 (2017). https://doi.org/10.1016/j.ijfatigue.2016.11.011
41. Wang, L., Qian, X.: Welding residual stresses and their relaxation under cyclic loading in welded S550 steel plates. Int. J. Fat. **162**, 106992 (2022). https://doi.org/10.1016/j.ijfatigue.2022.106992
42. Zarandi, E.P., Skallerud, B.H.: Experimental and numerical study of mooring chain residual stresses and implications for fatigue life. Int. J. Fat. **135**, 105530 (2020). https://doi.org/10.1016/j.ijfatigue.2020.105530
43. Schneider, T., Gibmeier, J., Kästner, M.: Experimental analysis of residual stress evolution under cyclic mechanical loading in 42CrMo4+QT (1.7225) including parametrization data. OpARA - Open Access Repository and Archive (2024). https://doi.org/10.25532/OPARA-288
44. Qvale, P., Zarandi, E.P., Arredondo, A., Ås, S.K., Skallerud, B.H.: Effect of cyclic softening and mean stress relaxation on fatigue crack initiation in a hemispherical notch. Fatigue Fract. Eng. Mat. Struct. **45**(12), 3592–3608 (2022). https://doi.org/10.1111/ffe.13834
45. Mathar, J.: Ermittlung von Eigenspannungen durch Messung von Bohrloch-Verformungen. Archiv für das Eisenhüttenwesen 6(7), 277–281 (1933) https://doi.org/10.1002/srin.193300416. _eprint: https://onlinelibrary.wiley.com/doi/pdf/10.1002/srin.193300416

46. Schajer, G.S., Whitehead, P.S.: Hole Drilling and Ring Coring. In: Practical Residual Stress Measurement Methods, pp. 29–64. John Wiley & Sons, Ltd (2013). https://doi.org/10.1002/9781118402832.ch2. Section: 2 _eprint: https://onlinelibrary.wiley.com/doi/pdf/10.1002/9781118402832.ch2
47. Brepols, T., Vladimirov, I.N., Reese, S.: Numerical comparison of isotropic hypo- and hyperelastic-based plasticity models with application to industrial forming processes. International Journal of Plasticity 63, 18–48 (2014) https://doi.org/10.1016/j.ijplas.2014.06.003
48. Kojic, M., Bathe, K.-J.: Studies of finite element procedures—stress solution of a closed elastic strain path with stretching and shearing using the updated Lagrangian Jaumann formulation. Comput. Struct. **26**, 175–179 (1987)
49. Trajkovic-Milenkovic, M., Bruhns, O.: Numerical analysis of finite hypo-elastic cyclic deformation with large rotations. Facta Univ. Arch. Civ. Eng. **17**(3), 299–313 (2019). https://doi.org/10.2298/FUACE190513006T
50. Xiao, H., Bruhns, O.T., Meyers, A.: The choice of objective rates in finite elastoplasticity: general results on the uniqueness of the logarithmic rate. Proc. R. Soc. Lond. A **456**(2000), 1865–1882 (2000). https://doi.org/10.1098/rspa.2000.0591
51. ABAQUS/Standard. Dassault Systemes. https://www.3ds.com/products/simulia/abaqus/standard
52. Simo, J.C.: On the computational significance of the intermediate configuration and hyperelastic stress relations in finite deformation elastoplasticity. Mech. Mater. **4**(3–4), 439–451 (1985). https://doi.org/10.1016/0167-6636(85)90039-0
53. Simo, J.C., Ortiz, M.: A unified approach to finite deformation elastoplastic analysis based on the use of hyperelastic constitutive equations. Comput. Methods Appl. Mech. Eng. **49**(2), 221–245 (1985). https://doi.org/10.1016/0045-7825(85)90061-1
54. Neto, E.A.d.S., Perić, D., Owen, D.R.J.: Computational Methods for Plasticity: Theory and Applications. Wiley, Chichester, West Sussex, UK (2008). OCLC: ocn209799487
55. Dafalias, Y.F.: The plastic spin concept and a simple illustration of its role in finite plastic transformations. Mech. Mater. **3**(3), 223–233 (1984). https://doi.org/10.1016/0167-6636(84)90021-8
56. Kobayashi, M., Ohno, N.: Implementation of cyclic plasticity models based on a general form of kinematic hardening. Int. J. Numer. Meth. Engng. **53**(9), 2217–2238 (2002). https://doi.org/10.1002/nme.384
57. Mathematica. https://www.wolfram.com/mathematica/
58. Korelc, J.: AceGen. http://symech.fgg.uni-lj.si/
59. Korelc, J., Wriggers, P.: Automation of Finite Element Methods. Springer, Cham (2016). https://doi.org/10.1007/978-3-319-39005-5
60. Wales, D.J., Doye, J.P.K.: Global optimization by basin-hopping and the lowest energy structures of lennard-jones clusters containing up to 110 atoms. J. Phys. Chem. A **101**(28), 5111–5116 (1997). https://doi.org/10.1021/jp970984n
61. Liu, D.C., Nocedal, J.: On the limited memory BFGS method for large scale optimization. Math. Program. **45**(1–3), 503–528 (1989). https://doi.org/10.1007/BF01589116
62. Beltrami, M., Pelegatti, M., Magnan, M., Lanzutti, A., Avdeev, M., Luzin, V., Leoni, M., De Bona, F., Salvati, E.: Microstructure and residual stress evolution during cyclic elastoplastic deformation of AISI316L fabricated via laser powder bed fusion. Materials Science and Engineering: A 898, 146416 (2024) https://doi.org/10.1016/j.msea.2024.146416
63. SIMULIA: ABAQUS 2022 User's guide
64. Balke, H.: Einführung in die Technische Mechanik. Springer-Lehrbuch. Springer, Berlin, Heidelberg (2010). https://doi.org/10.1007/978-3-642-10398-8